BAMS Article

Overview of the Chemistry in the Arctic: Clouds, Halogens, and Aerosols (CHACHA) Field Campaign

Jose D. Fuentes,[a] Sara Lance,[b] Kerri A. Pratt,[c] Paul B. Shepson,[d] William R. Simpson,[e] Izabella Antczak,[c] Katja Bigge,[f] Nathaniel Brockway,[e] Natasha Garner,[c] Kristian D. Hajny,[d] Daun Jeong,[c] Robert Kaeser,[d] Peter K. Peterson,[g] Miranda Serratos,[c] Tim Starn,[h] Brian H. Stirm,[i] and Sarah Woods[j]

KEYWORDS:
Arctic;
Aerosols;
Climate

ABSTRACT: The Chemistry in the Arctic: Clouds, Halogens, and Aerosols (CHACHA) field project aimed to advance the understanding of coupled meteorological and chemical processes in the atmospheric boundary layer during the seasonal increase in sea ice fracturing in spring. CHACHA sought to understand the interactions between this changing snow-covered surface, surface-coupled clouds, sea spray aerosols, multiphase halogen chemistry, and impacts of emissions from oil and gas extraction on atmospheric chemistry. The project measured greenhouse gases, reactive gases, size-resolved aerosol number concentrations, cloud microphysical properties, and meteorological conditions in real time, while also collecting particles for offline analysis. Two instrumented aircraft were deployed: the Purdue University Airborne Laboratory for Atmospheric Research and the University of Wyoming King Air. Flights were conducted out of Utqiaġvik, Alaska, between 21 February and 16 April 2022, sampling air over snow-covered and newly frozen sea ice in the Beaufort and Chukchi Seas, over open leads, and over the snow-covered tundra of the North Slope of Alaska, including the oil and gas extraction region near Prudhoe Bay. Observations showed that reactive bromine gases generally peaked near the snow-covered surface and decayed rapidly within the lowest few hundred meters where ozone was depleted, with concentrations reduced by nitrogen oxides emitted from oil fields. Cloud microphysical measurements revealed that thin clouds over and downwind of leads grew in vertical extent after contact with open water. Results from dropsondes indicated that convective boundary layers developed over leads, with depths ranging from 250 to 850 m depending on the fetch.

DOI: 10.1175/BAMS-D-24-0192.1
Corresponding author: Jose D. Fuentes, jdfuentes@psu.edu
Brockway's current affiliation: Air Quality Management District, Diamond Bar, California.
Garner's current affiliation: Department of Chemistry, University of Leeds, West Yorkshire, United Kingdom.
Jeong's current affiliation: Cooperative Institute for Research in Environmental Sciences, University of Colorado Boulder, Colorado and NOAA/Chemical Science Laboratory, Boulder, Colorado.
Supplemental information related to this paper is available at the Journals Online website: https://doi.org/10.1175/BAMS-D-24-0192.s1.
Manuscript received 12 July 2024, in final form 27 August 2025, accepted 5 September 2025

SIGNIFICANCE STATEMENT: Given the rapid pace of physical and chemical changes occurring in the Arctic, and the critical yet insufficiently understood roles of atmospheric turbulence, chemistry, and aerosol-cloud feedbacks, the Chemistry in the Arctic: Clouds, Halogens, and Aerosols (CHACHA) project aimed to enhance the understanding of the processes governing vertical variability of halogens and aerosols and, in turn, improve predictive capabilities for the Arctic's physical and chemical state, both now and in the future.

AFFILIATIONS: [a] The Pennsylvania State University, University Park, Pennsylvania; [b] Atmospheric Sciences Research Center, Albany, New York; [c] Department of Chemistry, University of Michigan, Ann Arbor, Michigan; [d] School of Marine and Atmospheric Sciences, Stony Brook University, State University of New York, Stony Brook, New York; [e] Geophysical Institute and Department of Chemistry and Biochemistry, University of Alaska Fairbanks, Fairbanks, Alaska; [f] Institute of Environmental Physics, Heidelberg University, Heidelberg, Germany; [g] Department of Chemistry, Whittier College, Whittier, California; [h] Department of Chemistry, West Chester University, West Chester, Pennsylvania; [i] Department of Aviation and Transportation Technology, Purdue University, West Lafayette, Indiana; [j] National Center for Atmospheric Research, Boulder, Colorado

1. Introduction

The Arctic is warming at a faster rate than anywhere else on Earth (Graham et al. 2017; Rantanen et al. 2022), with rapid changes driven by the cumulative effects of accelerated climate shifts and human activities in the region (Serreze and Barry 2011; Stuecker et al. 2018; Previdi et al. 2021; Shepson and Domine 2022). With declining sea ice extent and thickness, atmosphere–surface interactions are changing, which affects atmospheric boundary layer (ABL) thermodynamics, atmospheric composition, and cloud formation processes (Li et al. 2020). This warming is contributing to rapid perennial sea ice loss (Overland and Wang 2013), influencing sea ice dynamics (e.g., Stroeve and Notz 2018) and atmospheric features such as snowfall (Bintanja and Andry 2017). In many areas, springtime sea ice cover has transitioned from multiyear ice to thinner first-year ice, characterized by significant fracturing that results in the formation of leads, i.e., elongated channels of open water surrounded by ice (Richter-Menge and Farrell 2013). The width of leads varies from a few meters to several kilometers (Andreas et al. 1979; Smith et al. 1990; Lindsay and Rothrock 1995; Marcq and Weiss 2012; Tetzlaff et al. 2015; Gryschka et al. 2023). Arctic leads are developing in the middle of winter and early spring (Li et al. 2020), with an increasing frequency of wintertime sea ice fracturing in the Beaufort Sea (Rheinlænder et al. 2024). Open sea ice leads induce moist convective mixing and serve as a source of sea spray aerosols, cloud condensation nuclei (CCN), and water vapor that can enhance cloud formation (Radke et al. 1976; Smith et al. 1990; Orellana et al. 2011; Li et al. 2020). Water vapor, the most important greenhouse gas (Rodhe 1990), provides a positive feedback that augments regional atmospheric warming.

Changes at the Arctic surface are expected to be altering the natural multiphase halogen cycles (Pratt 2019). Reactive halogen species are produced and emitted into the atmosphere through a variety of biotic but mostly abiotic processes (Simpson et al. 2007b). Reactive halogen precursors include organohalogens such as bromoform ($CHBr_3$) and molecular halogens such as bromine (Br_2), chlorine (Cl_2), bromine chloride (BrCl), and iodine (I_2) (Foster et al. 2001; Pratt et al. 2013; Liao et al. 2014; McNamara et al. 2019; Raso et al. 2017; Custard et al. 2017).

Reactive halogen molecules influence the oxidative capacity of the ABL as they photolyze rapidly to produce halogen atoms, which then react with ozone (O_3), mercury (Hg), and hydrocarbons [including methane (CH_4)], thereby acting as important sinks for those chemical species (Barrie et al. 1988; Schroeder et al. 1998; Jobson et al. 1994; Simpson et al. 2007a; Steffen et al. 2008; Cavender et al. 2008; Saiz-Lopez and von Glasow 2012; Hornbrook et al. 2016; Wang et al. 2019; Benavent et al. 2022). The molecular halogens are also known to be produced within and emitted from sunlit snowpacks (Pratt et al. 2013; Custard et al. 2017; Raso et al. 2017), with these saline snowpacks, unique to the polar regions, being a key source of reactive bromine species (Jeong et al. 2022). Following polar sunrise, Br_2 molecules undergo photolysis to produce bromine (Br) atoms that rapidly react with O_3, leading to near-surface ozone depletion events (ODEs) in the ABL (Barrie et al. 1988; Simpson et al. 2007b; Wang et al. 2019). These events can last up to 12 consecutive days and lead to ozone-free air layers extending from the surface to as much as 2 km (Bottenheim et al. 2002; Helmig et al. 2012; Strong et al. 2002). Open sea ice leads increase convection, which, due to the associated upward and downward motions, can contribute to downward transport of O_3 from aloft to the surface. As a result, ozone-free air layers can be replenished with O_3, with the heterogeneity of the sea ice surface thought to contribute to the variability of the ODEs across spatial scales (Moore et al. 2014; Peterson et al. 2016).

Despite numerous previous field observations and important roles of halogen chemistry in various Arctic processes (Simpson et al. 2007b), most observations of halogen chemistry in the Arctic have been made at the surface and in coastal environments or obtained from satellite-derived retrievals of tropospheric column densities of bromine monoxide (BrO) (e.g., Platt and Wagner 1998; Richter et al. 1998; Seo et al. 2019; McNamara et al. 2020). However, numerical modeling studies underestimate of near-surface O_3 when Br_2 is parameterized using satellite-derived BrO columns (Wales et al. 2023), highlighting the need for vertically resolved reactive bromine measurements.

Low-vertical resolution observations of BrO from multiple-axis differential optical absorption spectroscopy (MAX-DOAS) measurements (Frieß et al. 2011; Peterson et al. 2015; Simpson et al. 2017) demonstrate that the vertical distribution of reactive bromine is highly variable and related to atmospheric stability and aerosol particle distribution. In addition to inducing convection to alter the vertical distribution of halogens, open leads are known sources of sea spray aerosols (Scott and Levin 1972; Radke et al. 1976; Nilsson et al. 2001; Leck et al. 2002; May et al. 2016; Kirpes et al. 2019), which may extend the vertical and horizontal scales associated with halogen chemistry. Airborne DOAS measurements during March 2012 showed the propagation of BrO within a lofted layer of coarse-mode aerosols (Peterson et al. 2017), although chemical composition measurements were not available to confirm the aerosol source. Ground-based observations via MAX-DOAS in the same study also indicated an association between lofted BrO and aerosol particles (Simpson et al. 2017). Increased cloud cover in the vicinity of leads, driven by the enhanced moisture source (Smith et al. 1990), can influence pollutant processing and the cycling of halogen species via multiphase reactions. However, such processes are not well understood, nor is the processing of aerosols by clouds. For example, the role of halogen chemistry in aqueous-phase reactions, such as sulfate formation within cloud droplets (Chen et al. 2017), remains underexplored.

Our understanding of the processes governing the chemical distribution and vertical variability of halogens, and their full spatial extent, from the ABL to the free troposphere, remains limited.

With sea ice loss, the Arctic is becoming more accessible to shipping and resource extraction (Allison and Bassett 2015; Harsem et al. 2015), leading to the development of infrastructure (e.g., paved and gravel roads, airports, pipelines, processing facilities, power plants, drill rigs, gravel pits, and pads) to support these activities, such as in Prudhoe Bay,

Alaska (Raynolds et al. 2014; Walker et al. 2022). In addition to impacting the surrounding natural environment in multiple ways (e.g., changes to soil physical properties, vegetation, permafrost, and snowmelt), these activities contribute to local Arctic combustion emissions of nitrogen oxides [NO_x = nitric oxide (NO) + nitrogen dioxide (NO_2)], sulfur dioxide (SO_2), volatile organic compounds (VOCs), and aerosols (Peters et al. 2011). These emissions of pollutants alter downwind atmospheric trace gas and aerosol composition (Custard et al. 2015; Gunsch et al. 2017; Kirpes et al. 2018; McNamara et al. 2019), as well as fog and cloud chemistry (Liu et al. 2021; Lata et al. 2023) and cloud properties (Maahn et al. 2017, 2021). However, combustion emissions in the Arctic and subsequent impacts on atmospheric composition (including halogen chemistry), clouds, and climate are highly understudied and largely unquantified (Schmale et al. 2018).

There is an urgent need to characterize the interactions between sea ice, open leads, snowpack, and atmosphere in the context of rapid environmental changes in the Arctic to improve current capabilities for predicting chemical composition and aerosol and cloud climate feedbacks. The Chemistry in the Arctic: Clouds, Halogens, and Aerosols (CHACHA) field project described in this article aimed to improve the understanding of how features such as leads and activities such as oil extraction impact the atmospheric thermodynamics and chemical composition of the Arctic ABL during spring, following polar sunrise. The CHACHA field campaign sought to evaluate three operational hypotheses to advance our knowledge of halogen chemistry and atmospheric thermodynamics in the Arctic ABL (Fig. 1). First, Arctic leads are sources of sea spray aerosols containing particulate halides, which affect cloud composition and the vertical and horizontal propagation of halogen chemistry. To test this hypothesis, we flew an aircraft (Fig. 2) within and above clouds over leads,

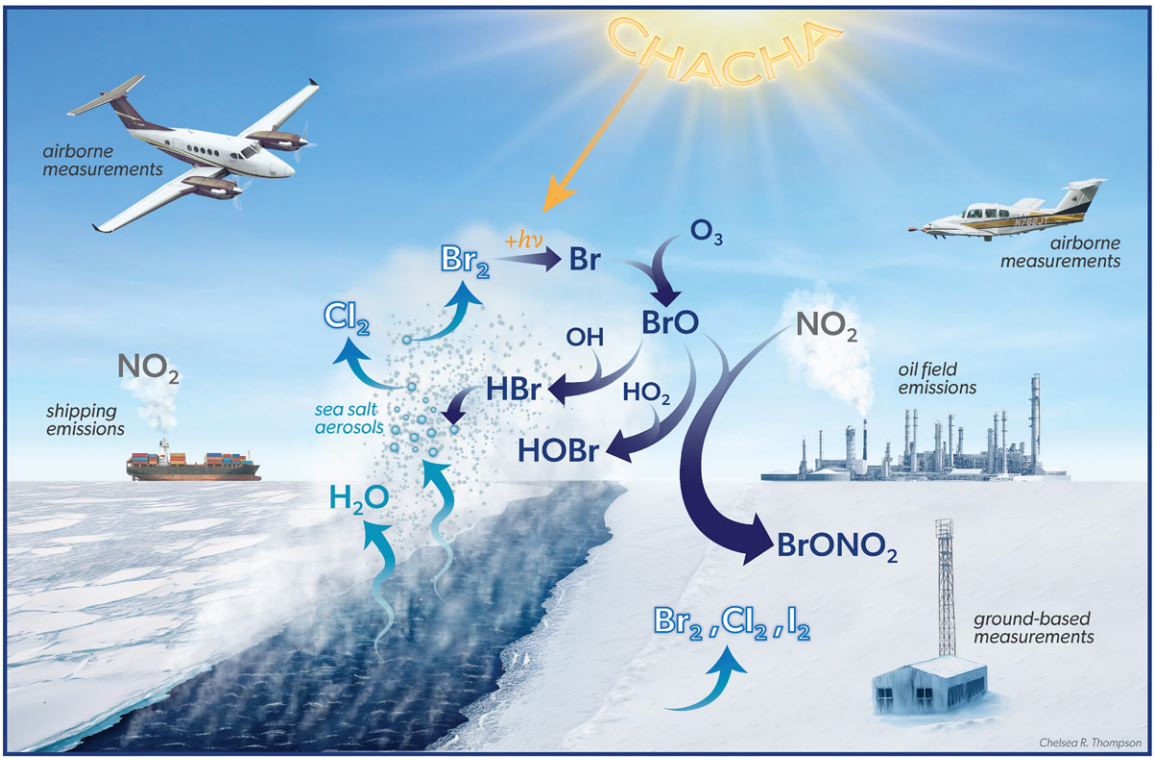

Fig. 1. Conceptual diagram illustrating the regions sampled by instruments on ALAR and King Air aircraft and key processes investigated during the CHACHA field campaign. As ice fractures and leads develop in late winter and early spring, warm and moist plumes transport sea salt aerosols and halogens (such as Br_2, Cl_2, I_2) to adjacent air layers. As gases such as Br_2 undergo photolysis, resulting Br atoms react with ozone, water vapor, and hydroxyl radicals, forming new molecules (e.g., BrO, HBr, and HOBr). In environments rich in nitrogen dioxide, these chemical cycles can be modified, resulting in the generation of pernicious reaction products such as $BrONO_2$.

Fig. 2. This picture shows the King Air and ALAR aircraft that were instrumented to sample air above sea ice, leads, and tundra for trace gases, particles, cloud constituents, and thermodynamic conditions in the ABL. Photo credit: Chris Rodgers.

as well as upwind and downwind of open leads, to measure trace gases, aerosols, and cloud composition, comparing these measurements to profiles over consolidated sea ice. Second, oil and gas extraction emissions substantially modify regional-scale natural halogen chemistry, impacting multiphase halogen recycling, as well as the fate of NO_x and O_3. We evaluated this hypothesis by flying two aircraft upwind and downwind of oil and gas extraction sites in Prudhoe Bay, Alaska, and comparing measurements of gas and particle-phase halogens, as well as NO_2 and O_3, to those upwind measurements (Fig. 3). Third, atmospheric oxidative processing of nitrogen and other chemical species differs between clear-sky conditions and those impacted by in-cloud chemical processing. To test this hypothesis, the composition of cloud residual particles was compared at different locations above and downwind of open sea ice leads and further contrasted with the gas and particle composition upwind of the leads.

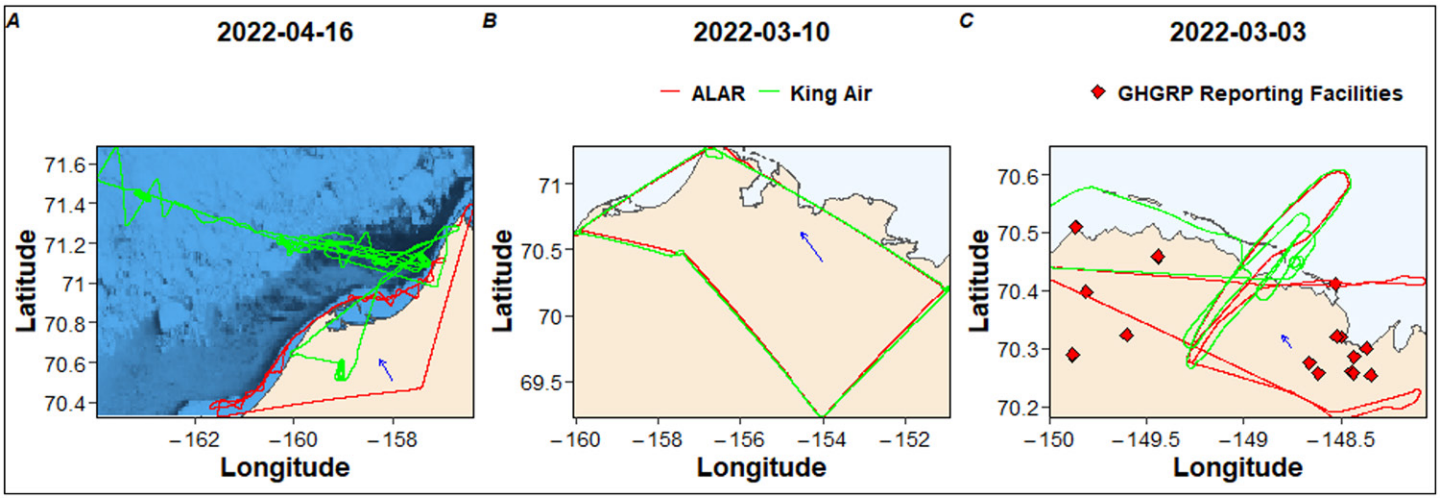

Fig. 3. Examples of aircraft flight tracks are shown to demonstrate the spatial extent of air sampling during the CHACHA campaign. The insets show the flight transects for air sampling: (a) above leads and sea in the Chukchi Sea, (b) over the North Slope snow-covered tundra, and (c) over and downwind of the Prudhoe Bay oil and gas fields. Blue arrows indicate the prevailing wind direction.

2. The CHACHA field campaign

The CHACHA field campaign took place from mid-February to mid-April 2022 and was based out of Utqiaġvik, Alaska, located at the northernmost point of the state between the Chukchi and Beaufort Seas (see Fig. 3). The University of Wyoming King Air and the Purdue University Airborne Laboratory for Atmospheric Research (ALAR) aircraft (Fig. 2) served as airborne platforms to carry the necessary instrumentation (Table 1) for physical and chemical measurements of gases, particles, and cloud droplets, as well as measurements of winds and air turbulence, and to investigate the states of ABL thermodynamics. In addition, a tundra site provided continuous ground-based measurements of O_3 and sampling of particles and snow (Table 1) to further connect surface conditions to the flight data. The King Air deployment consisted of 33 research flights to sample the air and gather data, including profiles and low approaches at nearby airports, with a focus on clear weather days. A portion of these flights targeted clouds that formed over leads in the sea ice. The ALAR completed 24 flights, including nine Prudhoe Bay flights, six survey flights, and nine lead flights.

The ALAR aircraft is a modified twin-engine Beechcraft Duchess with an operational airspeed of 66 m s^{-1}. A global positioning system (GPS)/inertial navigation system (INS) unit provided the aircraft's position at 50 Hz. At the front of the aircraft (Fig. 2), we mounted a best air turbulence (BAT) probe that recorded three-dimensional wind speed measurements at 50 Hz, following previous procedures (Garman et al. 2006, 2008). Two temperature probes were operated at frequencies of 0.5–1 Hz to measure ambient temperature. A pyranometer (model LI-200SA, LI-COR Environmental, Lincoln, Nebraska) recorded incoming solar irradiance at a frequency of 50 Hz. Additional instruments included an O_3 gas analyzer (model 205, 2B Technologies, Broomfield, Colorado) to measure the 10-s average O_3 mixing ratio. A particle counter (model 1.109, Grimm Aerosol Technik, Hamburg, Germany) recorded size-resolved distributions (from 0.25 to 30 μm) every 6 s. An integrated cavity output spectroscopy (ICOS) gas analyzer (model 911, Los Gatos Research, Mountain View, California) measured NO_2 at 1 Hz, while a cavity ring-down spectrometer (model G2301-m, Picarro Inc., Santa Clara, California) recorded ambient levels of carbon dioxide (CO_2), CH_4, and water vapor at 0.5 Hz, according to previous measurement protocols (Crosson 2008), calibrated with National Oceanic and Atmospheric Administration (NOAA) certified compressed gas standards. A DOAS instrument, called the Heidelberg Imaging DOAS Instrument (HAIDI; General et al. 2014), was also installed in the ALAR aircraft for forward and nadir slant column measurements of BrO and NO_2 (Brockway et al. 2024), from which the vertical air column gas density and concentrations as a function of altitude were obtained for these two gases. Hajny et al. (2025) and Brockway et al. (2024) provide details about the calibration protocols for the instruments and data quality control procedures.

The King Air research aircraft was equipped with a manual dropsonde launch tube to release dropsondes (model NRD41, NCAR, Boulder, Colorado), which utilized a square-cone parachute to reduce the initial shock load and to slow and stabilize the dropsondes as they descended. The manual dropsonde launcher was installed toward the aft of the King Air and operated by the flight scientist. The parachute deployed immediately upon exit from the launch chute and became stable after opening, eliminating any pendulum motion during the descent of dropsondes. We followed unique flight transect strategies to study atmospheric thermodynamics over leads using dropsondes. We released several dropsondes over the leading edge of leads, over the open water of leads, and over the downwind of leads. To initiate dropsonde releases, the King Air aircraft spiraled upward to reach the desired altitude of 3.5 km above the surface. The aircraft then cruised at a constant altitude and released the dropsondes along the required transect to measure air thermodynamics as dropsondes descended from 3.5 km to the surface (Fig. 3). Dropsonde humidity sensors were reconditioned before launch to reduce the potential for humidity contamination, ensuring optimal

Table 1. Description of instruments employed during the CHACHA field campaign and the environmental variables measured. Instruments operated during mid-February–mid-April 2022.

Instrument	Variable	Measurement frequency	Height or depth (m)	Aircraft
	Meteorological sensors			
Thermistor	Air temperature (Tair)	0.5 Hz	Profiles	ALAR
Hygristor	Relative humidity (RH)	0.5 Hz	Profiles	ALAR
BAT probe	Wind speed (u, v, w)	50 Hz	Profiles	ALAR
Pyranometer	Incoming solar irradiance	1 Hz	Profiles	King Air
Pyrgeometer	Incoming terrestrial irradiance	1 Hz	Profiles	ALAR, King Air
Rosemount probe	Pressure, temperature, RH	50 Hz	Profiles	King Air
Dropsondes	Pressure, Tair, RH, u, v	1 Hz	Profiles	King Air
Applanix AV-410	Aircraft position and attitude	1 Hz	Profiles	King Air
Rosemount HADS, CPT-6140	Static pressure	25 Hz	Profiles	King Air
Rosemount 102	Air temperature	25 Hz	Profiles	King Air
Rosemount 0858	Airflow	25 Hz	Profiles	King Air
Edgetech Vigilant 137	Water vapor	25 Hz	Profiles	King Air
King KRA 405B	Radar altitude	25 Hz	Profiles	King Air
Rosemount 1332	Cabin pressure	25 Hz	Profiles	King Air
	Aerosol and gas analyzers			
PCASP SPP-100	Aerosol size distribution	1.0 Hz		King Air
POPS	Aerosol size distribution	1.0 Hz		King Air
GRIMM	Aerosol size distribution	6.0 s		ALAR
CPC	Aerosol number concentration	1.0 Hz		King Air
CDP	Cloud droplet sizes	1.0 Hz		King Air
2D-S	Cloud particle sizes	1.0 Hz		King Air
PILS	Particle inorganic ion composition (offline ion chromatography)	3-min samples		King Air
DRUM	Single particle size and composition (offline microspectroscopy)	~30-min samples		King Air
CIMS	Reactive gases	5-s cycle		King Air
2B Ozone	Ozone	1 s		ALAR, King Air
HAIDI	BrO, NO_2	1 s		ALAR
Picarro	Methane	1 s		ALAR
	Ground-based sensors			
Model 49i	Ozone	1 Hz	2	
APS 3321	APS	1 min	2	
OPS 3330	OPS	1 min	2	
SMPS 3910	SMPS		2	
DRUM	Particle inorganic ion composition (offline ion chromatography)	Daily	2	
MOUDI	Single-particle size and composition (offline microspectroscopy)	Daily	2	
Snow	Snow sampling (offline ion chromatography)	Daily	Surface	

measurement performance throughout the entire altitude and temperature range of profiles. The Airborne Vertical Atmospheric Profiling System (AVAPS) software system received and stored data from dropsondes.

The King Air operated in one of two different configurations based on goals and conditions expected for each flight because power limitations prevented the full payload from

operating all at once. For clear air-focused flights, a chemical ionization mass spectrometer (CIMS; THS Instruments; Neuman et al. 2010; Liao et al. 2011) and an O_3 gas analyzer (model 205, 2B Technologies Inc.) were powered on, while the cloud probes and counterflow virtual impactor (CVI) inlet [Brechtel Manufacturing Inc. (BMI), Hayward, California; Shingler et al. 2012] were powered off. Conversely, for cloud-focused flights, the cloud probes and CVI were powered on, while the CIMS and O_3 instruments were powered off. Aerosol measurements were conducted on all flights. The King Air was equipped with a wing-mounted passive cavity aerosol spectrometer probe [PCASP; Droplet Measurement Technologies (DMT)], which measures ambient aerosol size distributions for particle diameters between 0.1 and 3 μm. The King Air was also equipped with a Rogers inlet (manufactured at the University of Wyoming) for sampling aerosols in clear air, as well as the aforementioned CVI for in-cloud sampling and subsequent measurements of cloud droplet residuals, i.e., the particles remaining upon evaporation of water from cloud droplets. A high flow three-way valve (BMI) was used to switch between the Rogers inlet and CVI while in flight. Sampling from these inlets, continuous aerosol instruments within the King Air cabin included a portable optical particle spectrometer (POPS; Handix Scientific, Fort Collins, Colorado; Gao et al. 2016), providing particle size distributions (PSDs) for diameters between 0.13 and 3 μm, and a condensation particle counter (CPC) for total aerosol number concentrations. A particle-into-liquid sampler (PILS; BMI; Orsini et al. 2003) collected particles with ~3-min time resolution in Milli-Q water, following denuder-based removal of acidic gases from the airstream, for offline ion chromatography measurements of particulate inorganic ion composition. A three-stage Davis rotating-drum universal-size-cut monitoring (DRUM) impactor (DELTA 3-DRUM, DRUMAir, LLC) (Cahill et al. 1987; Olson et al. 2019) collected particles with variable time resolution (~5–30 min) for offline scanning electron microscopy (SEM) with energy-dispersive X-ray (EDX) spectroscopy measurements of single-particle size and elemental composition.

During clear-air flights, the CIMS measured atmospheric Br_2 (+HOBr), cyanogen bromide (BrCN), nitric acid (HNO_3), and peroxynitric acid (HO_2NO_2) with a 5-s duty cycle using iodide-water clusters [$I(H_2O)^-$] as the reagent ion (Liao et al. 2011). Ambient measurements were conducted by sampling < 1 L min^{-1} (LPM) continuously throughout the flight with an excess flow of 3.8 LPM to reduce residence time in the inlet. The ion molecular reaction (IMR) chamber was kept at a constant pressure (20 Torr) by controlling ultrahigh purity (UHP) nitrogen through the IMR. The air was sampled through heated (40°C) ½″ OD Teflon tubing. In-flight calibrations were performed using an online Br_2 source in a permeation tube (VICI Metronics) heated to 50°C. The output of the Br_2 permeation source was quantified regularly in the field (Liao et al. 2011). A custom-made pneumatic valve was used to switch between ambient and background sampling (Liao et al. 2011). Background measurements were obtained by flowing ambient air through a heated (40°C) charcoal filter with glass wool at both ends. Quantification of each measured gas species was achieved by using the relative sensitivities of each calibrated compound to Br_2, determined in the laboratory after the campaign.

To obtain measurements of cloud microphysical properties, the King Air was equipped with an externally mounted cloud droplet probe [CDP; DMT, Longmont, Colorado; Lance et al. 2010, 2011] and 2-dimensional stereo probe [2D-S; Stratton Park Engineering Company (SPEC), Inc., Boulder, Colorado; Lawson et al. 2006]. The CDP, a forward scattering spectrometer, provided the number concentration of cloud droplets as a function of droplet diameter in the range 2–50 μm, and this particular instrument was modified with a pinhole on the sizing detector to limit coincidence artifacts (Lance 2012) and calibrated in the laboratory with water droplets of known size prior to the CHACHA deployment (Faber et al. 2018). The 2D-S, an optical array probe, measured the concentration, size, and cross-sectional area of cloud particles with diameters between about 10 μm and 2 mm, and this particular

instrument was configured with sharp tips to limit ice shatter artifacts (Lawson 2011). The 2D-S also provided shadowgraph-type imagery of particles that can be used to provide an indication of particle phase and ice crystal habit.

We designed and followed different aircraft flight trajectories and transects (Fig. 3) for air sampling of gases and aerosols. We conducted many flights with both aircraft flying the same (or similar) track, while some involved separate flights, based on research hypotheses. Specifically, the ALAR aircraft was better outfitted for vertical profile measurements of gases, while the King Air was better equipped for studying open leads and their impacts on aerosols and clouds. In Fig. 3, we show three sets of example flight tracks—one in and around the oil fields of Prudhoe Bay, where several flights were conducted by flying two transects at different altitudes and fixed downwind distances, for the determination of NO_x, CO_2, and CH_4 emission rates. Whenever possible, flight transects were aligned perpendicular to the mean wind direction to optimize the aircraft mass balance approach for measuring emission rates, as described in Hajny et al. (2025) and references therein. Additionally, flight patterns followed upward and downward spirals to measure gas concentrations, temperature, and air turbulence profiles in the ABL. The altitudes of passes downwind of the oil fields sampled air throughout the ABL, whose maximum statically stable depth reached 300–400 m. Aircraft air sampling extended from approximately 50 to 3500 m above the surface. Flights also included transects to sample air within the ABL upwind of Prudhoe Bay to ensure air sampling included background conditions outside the influence of the oil fields. Flight transects took place over the Beaufort Sea, the tundra in and around and to the south of Utqiaġvik, and the Chukchi Sea to study trace gas and aerosol concentrations and investigate chemical processes (Fig. 3). Several flights performed air sampling within and outside of clouds to investigate cloud droplet characteristics (size and concentration) and chemical composition.

Ground-based measurements were made during the CHACHA field campaign at a station located approximately 3 km east of the city of Utqiaġvik, Alaska, to investigate the temporal dynamics of trace gases and particles. A gas analyzer (model 49i, Thermo Fisher Scientific Inc., Franklin, Massachusetts) continuously measured O_3 at a frequency of 1 Hz. An aerodynamic particle sizer (APS; model 3321, TSI Inc., Shoreview, Minnesota) measured particle sizes with high resolution, ranging from 0.5 to 20 μm. Particle concentration and particle size distribution, ranging from 0.3 to 10 μm, were measured at a frequency of 0.017 Hz using an optical particle sizer (OPS; model 3330, TSI Inc.). A scanning mobility particle sizer (SMPS) spectrometer (model 3910, TSI Inc.) recorded ambient particles in the 10–420-nm range. Aerosols were sampled through 3-m-long, antistatic tubing (3/16-in. outer diameter and 1/8-in. inner diameter) from inlets placed 2 m above the surface, outside a temperature-controlled housing unit that contained the instruments. Atmospheric particles were collected with daily time resolution using two size-resolved aerosol impactors. A 10-stage rotating microorifice uniform deposit impactor (MOUDI; model 120R, MSP Corp.) collected particles on silicon substrates (Ted Pella, Inc.) for the electron microscopy analysis. A three-stage DRUM impactor (Cahill et al. 1987) collected particles on a fluoropore membrane (3.0-μm pore size, hydrophobic polytetrafluoroethylene, Millipore Sigma) for the ion chromatography analysis. Snow resting on the surface (~2 cm in depth) was sampled daily at the tundra site using a polypropylene scoop, stored double bagged in polyethylene bags, and kept frozen at −40°C for the ion chromatography analysis.

3. Highlights from CHACHA

The CHACHA project began shortly after the polar sunrise as revealed by the low levels of incoming solar radiation, which reached only tens of watts per square meter in early February and steadily increased over time due to the seasonal progression from winter to

spring (Fig. 4). Outgoing terrestrial radiation (L_{up}) from the snow-covered surface showed minimal variability, remaining around 260 W m^{-2}, consistent with persistently cold surfaces. In contrast, incoming terrestrial radiation (L_{dwn}) ranged from 125 to 280 W m^{-2}, reflecting variability in cloud cover and atmospheric water vapor content. This variability is reflected in the observed trend in specific humidity (Fig. 4), which remained below 0.5 g kg^{-1} early in the measurement period and increased to 1.5–2.0 g kg^{-1} toward the end of the field campaign.

Net radiation remained predominantly negative, with a minimum of –100 W m^{-2} in early February, and gradually increased over time (Fig. 4). Around day 110 (20 April 2022), net radiation became positive, indicating a seasonal energy surplus that enabled surface warming. This energy shift was consistent with the air temperature trend, which initially dropped below –30°C and gradually increased over the period, approaching 0°C by day 120. For much of February, low wind speeds prevailed due to stagnant, cold air masses

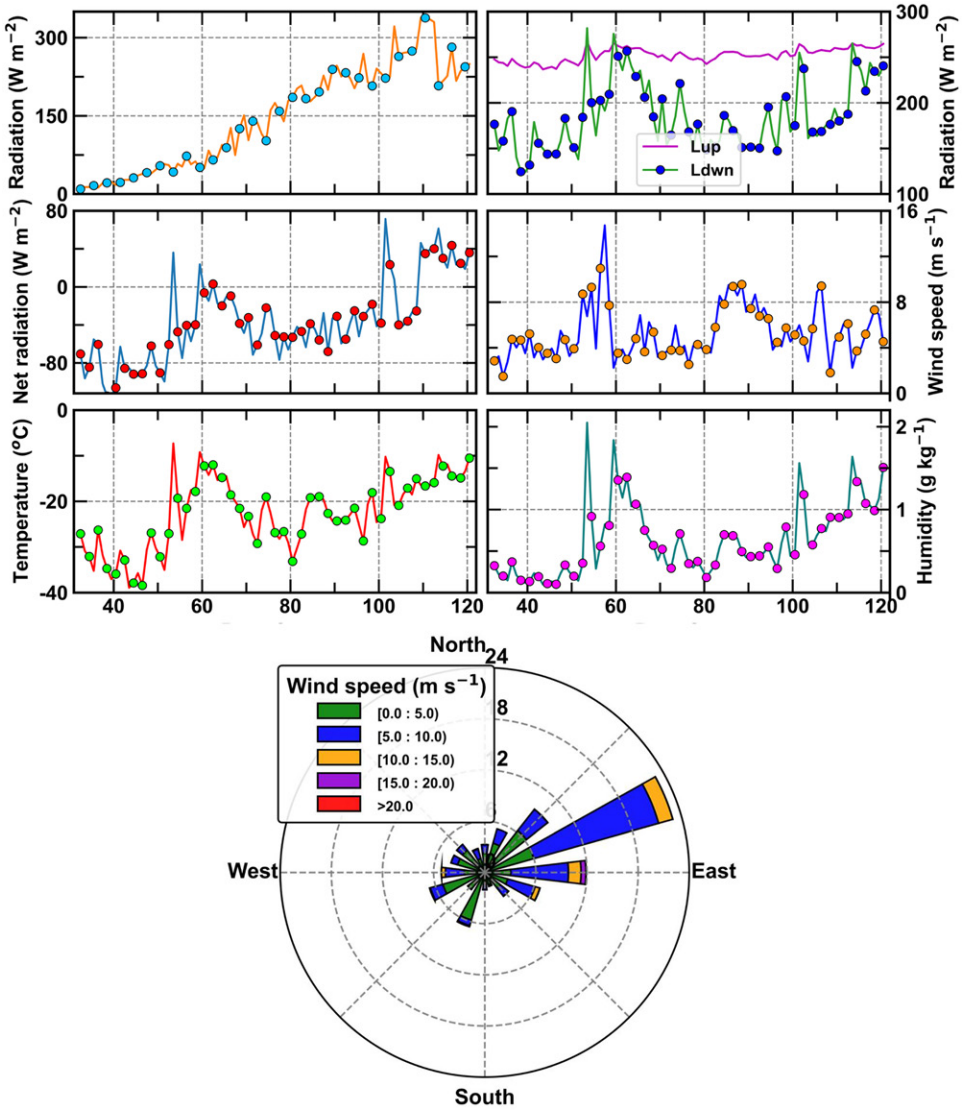

Fig. 4. This figure provides a summary of the meteorological conditions observed at the NOAA Observatory in Utqiaġvik, Alaska, from February to April 2022 (day 32–day 120 of the year), based on daily averaged values. Symbols represent data plotted every other day, with lines connecting the daily means. The figure includes (top left) incoming solar radiation (W m^{-2}), (top right) downwelling (L_{dwn}) and upwelling (L_{up}) longwave radiation (W m^{-2}), (middle left) net radiation (W m^{-2}), (middle right) wind speed (m s^{-1}), (bottom left) air temperature (°C), and (bottom right) specific humidity (g kg^{-1}). Wind rose: distribution of wind direction and speed for the same period. Each bar indicates the frequency of winds from a specific direction, with colors denoting wind speed values (m s^{-1}).

confined within the Arctic region (see Figs. S1–S3 in the online supplemental material). In late February (day of year 52–60), wind conditions became more turbulent, with daily average speeds reaching up to 15 m s^{-1}, likely associated with storm events or frontal passages. The wind direction was predominantly from the east-northeast (ENE), as shown in the wind rose (bottom plot, Fig. 4), with most wind speeds falling in the 5–10 m s^{-1} range (blue) and occasional events exceeding 10 m s^{-1} (yellow and magenta). Calm conditions (<5 m s^{-1}, green) occurred in all directions but were least common from the dominant ENE sector. Synoptic conditions and vertical cross sections of potential temperature are summarized in Figs. S1–S9. Longitudinal (from 165° to 145°W) and latitudinal (from 60° to 80°N) vertical cross sections of potential temperature along latitude 71.29°N are based on ERA5 reanalysis data and span pressure levels from 1000 to 800 hPa. Together, these atmospheric conditions (Fig. 4, Figs. S1–S9) provide critical context for understanding the spatial and temporal variability in atmospheric thermodynamics and trace gas concentrations observed during the CHACHA field campaign.

During February and early March 2022, near-surface O_3 levels showed little variability (Fig. 5). In late February, the variability of O_3 progressively increased in response to the more active halogen-catalyzed photochemical destruction, episodic turbulent transport (see wind speed, Fig. 4) of ozone-laden air from aloft, and increasing actinic flux from rising solar radiation (Fig. 4). For example, in March 2022 (day of year 60–65), O_3 levels ranged from 10 to 45 ppb due to the enhanced photochemical loss and intermittent mixing with background air. As the solar zenith angle decreased through March, photochemistry activity in the ABL intensified, further increasing O_3 variability. By mid-March 2022, the ODEs became evident as O_3 levels dropped to less than 10 ppb for several consecutive hours (Fig. 5, see histogram for March). The ODEs manifested as rapid decreases in O_3 levels from about 40 ppb to as low as 0.5 ppbv. The duration of ODEs ranged from 3 to 4 h to several days, consistent with prior observations at Utqiaġvik (e.g., Oltmans et al. 2012; Moore et al. 2014; Halfacre et al. 2014;

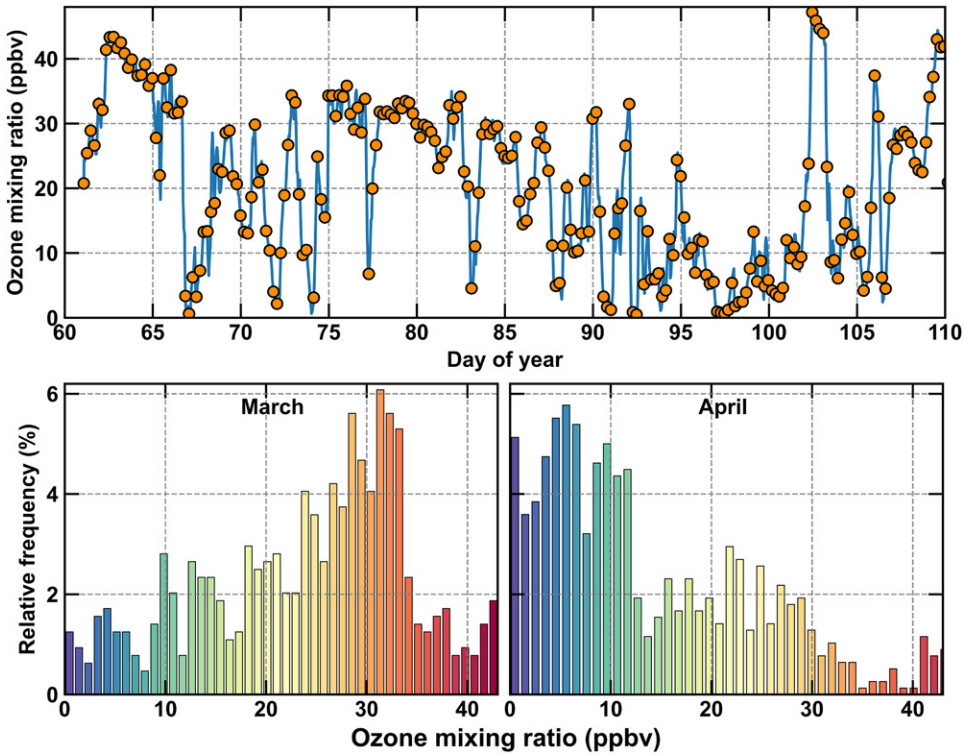

Fig. 5. Ground-level ozone was measured at Utqiaġvik, Alaska, during 2022. (top) Hourly ozone mixing ratios measured during the CHACHA measurement period from day of year 60 (1 Mar) to 105 (15 Apr) in 2022. (bottom) Ozone relative frequency distributions for (left) March and (right) April, with histogram bins shaded by 1-ppb intervals.

Widmaier et al. 2024). The most pervasive and intense ODEs occurred in April 2022, when O_3 levels remained below 10 ppb for about 35% of the time (Fig. 5, see histogram for April) due to the dominance of halogen chemistry during this period (Bottenheim et al. 1993; Oltmans and Komhyr 1986; Foster et al. 2001; Bottenheim et al. 2002; Oltmans et al. 2012; Jeong et al. 2022).

Throughout the CHACHA campaign, the ALAR aircraft performed "porpoising" maneuvers, during which the airplane flew constant-rate ascents/descents from near surface to above the top of the ABL (~600–1000 m). Results for O_3 and BrO are shown in Figs. 6a–d, for two sample flights done on 10 March 2022 and 12 April 2022. Figure 6a illustrates the vertical variability of O_3 from Wainwright to the west and to the east (not quite as far as Prudhoe Bay) and over the tundra snowpack. On the west side, O_3 was depleted below ~100-m altitude, where halogen chemistry and O_3 depletion were active, reducing O_3 to less than 10 ppb, but it increased to up to 50 ppb above the surface layer, where O_3 levels were near background. On 10 March, a stagnant cold air mass with temperatures below 255 K dominated the region around Utqiaġvik, characterized by steeply sloping longitudinal isentropes toward the

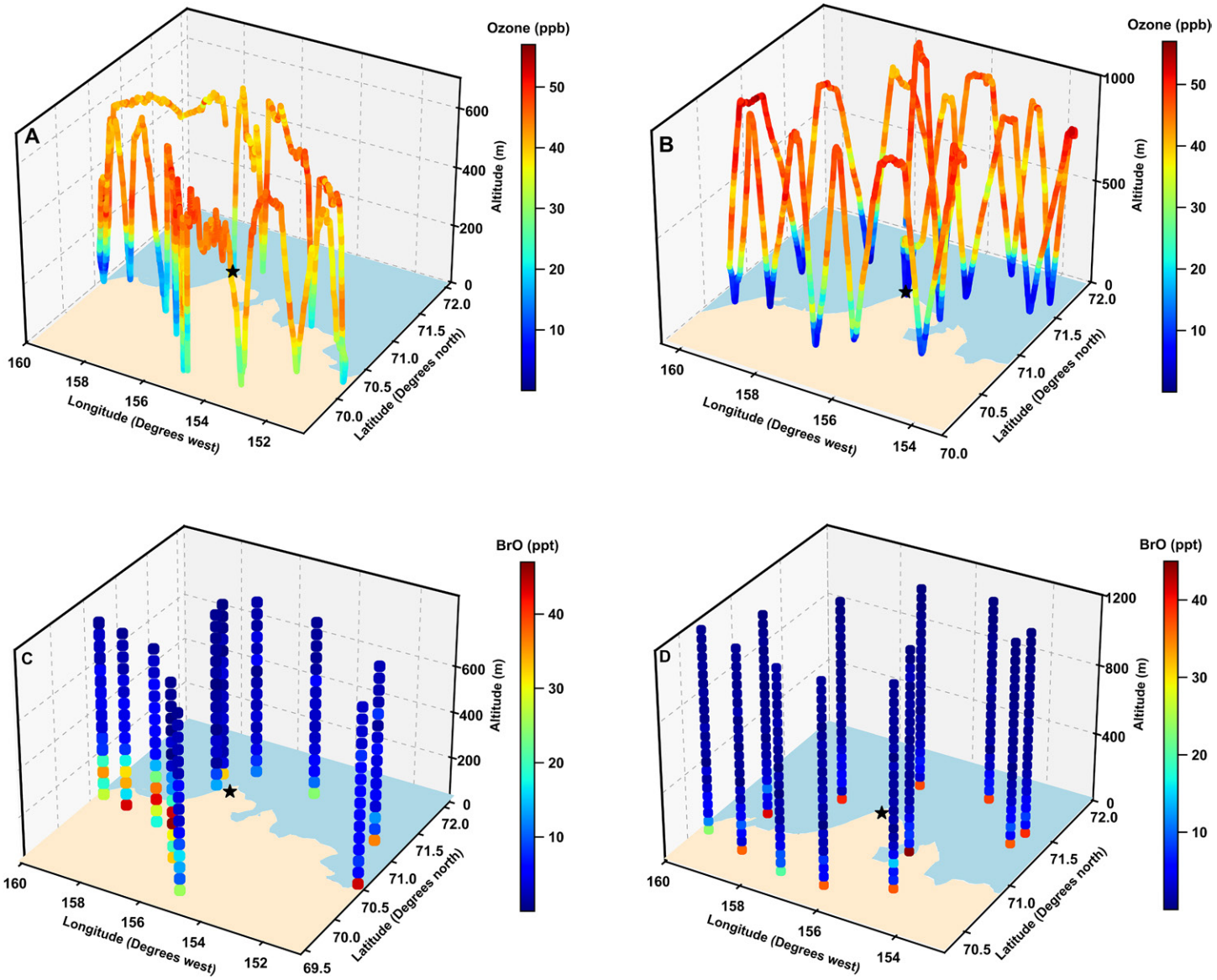

Fig. 6. Vertical and horizontal variations in ozone measured over sea ice and the North Slope snow-covered tundra on (a) 10 Mar 2022 and (b) 12 Apr 2022. The results showed occurrences of ozone depletion events (ozone levels < 10 ppb), which mostly affected the air layer from the surface to about 400 m. (c),(d) The corresponding results for BrO indicated that the ozone-depleted air layers exhibited elevated mixing ratios of BrO, the product of the reaction of Br_2 atoms with ozone.

northeast and a pronounced cold pool south of Utqiaġvik (Figs. S10–S12). The 12 April 2022 profiles (Fig. 6b) include O_3 vertical variability measured over both the North Slope tundra, as well as two cases over the Chukchi Sea to the west and several profiles over the Beaufort Sea to the east. All profiles show similar patterns: near 0-ppb O_3 close to the surface and up to ~50 ppb above the depleted surface layer. There is no clear distinction in O_3 vertical variability between areas over the frozen ocean and over the tundra. BrO vertical profiles retrieved from airborne imaging DOAS measurements are plotted as averages for 50-m thick air layers (Figs. 6c,d). On 12 April, an air mass with temperatures 260–265 K dominated the region around Utqiaġvik, characterized by sloping longitudinal isentropes toward the southwest and a cold pool over the central Arctic Ocean (Figs. S13–S15). Near the surface (<50 m), the BrO mixing ratio reached as high as 50 ppt and then quickly decreased to <10 ppt in the air layers aloft (>225 m). The vertically resolved profiles for BrO are described in detail in Brockway et al. (2024), with BrO most frequently observed to be enhanced near the surface. The highest measured column BrO cases had, on average, 56% of the BrO in the lowest 200 m (Brockway et al. 2024), similar to the ground-based results reported by Peterson et al. (2015). Based on the representative flight shown in Fig. 6 and full campaign results described by Brockway et al. (2024), bromine chemistry is most often revealed to be a near-surface phenomenon. However, as discussed in Brockway et al. (2024), there were cases in which reactive bromine was lofted to higher altitudes (200–300 m), for which the highest lower-tropospheric vertical column densities of BrO were observed (as in Fig. 6c), although these were observed infrequently (6% of retrievals during CHACHA). The enhanced near-surface BrO is consistent with snowpack sources of reactive bromine, as discussed in detail in previous studies (Foster et al. 2001; Pratt et al. 2013; Custard et al. 2017; Wang et al. 2019; Ahmed et al. 2022; Jeong et al. 2022).

There are several processes related to oil and gas production, as well as electric power production for various uses in the Prudhoe Bay oil fields, that involve combustion, resulting in emissions of NO_x (Jaffe et al. 1995). At various times during this study (King Air had nine and ALAR completed nine Prudhoe Bay flights), we flew downwind of Prudhoe Bay and measured NO_2 as described in Hajny et al. (2025). In Fig. 7, we show one case of the vertical distribution of CO_2 and NO_2 measured downwind of the Prudhoe Bay oil fields. Ambient NO_2 levels as high as 67 ppb were measured in air layers near the surface (~120 m; Hajny et al. 2025), while NO_2 levels in background air in the Arctic were typically <0.050 ppb. As discussed in previous studies (Custard et al. 2015), the enhanced NO_2 level can react with BrO to produce $BrONO_2$, acting as a radical termination step and decreasing the efficiency of the bromine radical reaction cycles. The increased reaction of NO_2 with Br radicals and BrO suppresses HOBr formation, although the resulting bromo nitrite ($BrNO_2$) and $BrONO_2$ can also react further to contribute to the reactive bromine cycling (i.e., formation of Br_2) (Wang and Pratt 2017; Wang et al. 2019). The influence of NO_2 on the regional bromine chemistry is shown in Fig. 8 and discussed by Brockway et al. (2024), demonstrating the column abundance of both NO_2 and BrO that resulted from a "rastering" flight using the HAIDI mapper over the Prudhoe Bay oil fields. It is evident that BrO is greatly diminished in point source plumes that have more NO_2 (Fig. 8). These impacts persist beyond the North Slope of Alaska oil fields, leading to observed reductions in BrO 300-km downwind (Peterson et al. 2025).

We hypothesize that sea spray aerosol from open sea ice leads acts as cloud droplet nuclei above and downwind of the leads as supported by prior cloud condensation nuclei measurements (Radke et al. 1976) at Utqiaġvik. Figure 9 shows the SEM image and corresponding EDX spectroscopy spectra of a representative individual organic-coated sea salt aerosol particle, collected at the tundra ground site in April, when open sea ice leads were present in both the Beaufort and Chukchi Seas. The morphology and elemental composition of this example

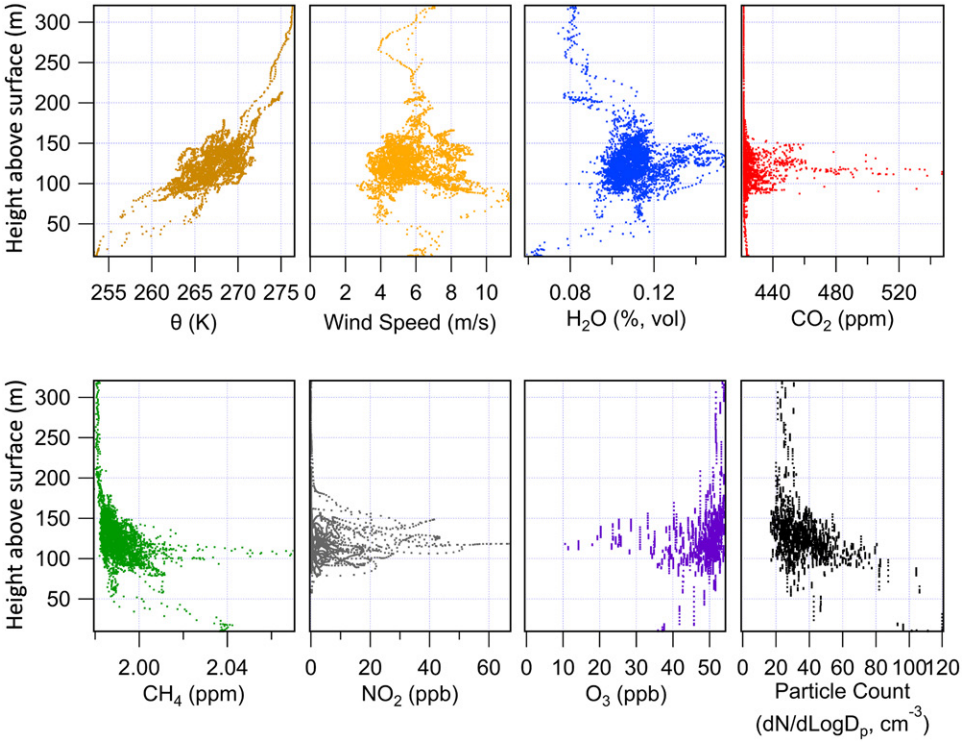

Fig. 7. Vertical variation of potential temperature θ, wind speed, H_2O mixing ratio, CO_2 mixing ratio, CH_4 mixing ratio, NO_2 mixing ratio, O_3 mixing ratio, and particle concentration measured downwind of Prudhoe Bay on 27 Feb 2022. A plume laden with trace gases and particles was observed in the air layer between 50 and 200 m above the surface, with NO_2 levels reaching 57 ppb and O_3 ranging from ~10 to 50 ppb, likely associated with emissions from the oil fields.

particle is consistent with nascent (nonchloride depleted) sea spray aerosol produced during marine aerosol generation experiments in the Arctic pack ice using locally collected seawater (Mirrielees et al. 2024). It is also consistent with prior SEM-EDX measurements of sea spray aerosol at Utqiaġvik (Kirpes et al. 2018, 2019; Chen et al. 2022).

We extensively sampled clouds upwind, directly overhead, and downwind of leads. We observed stratiform and shallow clouds, with vertical thicknesses often ranging from 150 to 300 m. Cloud bases were lower closer to the leads, with the lowest clouds appearing to

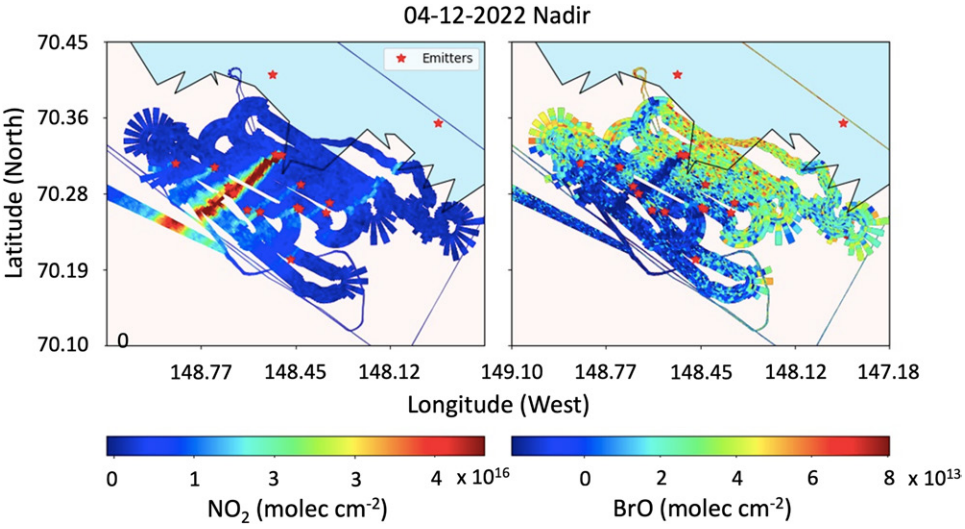

Fig. 8. Spatial variability of (left) nitrogen dioxide and (right) bromine monoxide column densities, measured in and around the Prudhoe Bay oil fields. The symbol * denotes the locations of facilities responsible for the anthropogenic emissions of gases and particles.

emanate from open leads as reduced visibility patches referred to as "sea smoke" (Saunders 1964), sampled at altitudes of 90–150 m above the surface. Based on clouds sampled with aircraft instruments, cloud tops reached heights of 300–500 m. Cloud height generally increased with distance downwind of leads (Fig. 10). Cloud-top temperatures typically ranged from −22° to −16°C. While flight conditions were smooth outside of clouds, the air became quite turbulent within the clouds, with updrafts and downdrafts often reaching speeds of 2–3 m s^{-1}. Regarding cloud phase, some segments were fully glaciated, while most clouds were mixed phase, with pockets of supercooled liquid water mixed with ice particles. Given the varied conditions, ice present in these mixed-phase clouds could have been induced by primary formation mechanisms or in several instances by seeding from blowing snow or sedimentation from midlevel clouds. Detailed assessment of such mechanisms will be included in forthcoming publications. The liquid water content of the clouds ranged from 0.05 to 0.1 g m^{-3}, with some reaching as high as 0.2 g m^{-3}. Ice crystals were mostly irregular in shape, although occasional columns or other faceted habits were observed. The cloud particle size distribution commonly exhibited bimodal patterns (Fig. 10). Cloud droplets had narrow size ranges, with peak values varying from 6 to 13 μm, close to the CVI cutoff size. Ice particles displayed a broader size distribution, extending from approximately 100-μm to as large as 1-mm diameter in some cases (Fig. 10).

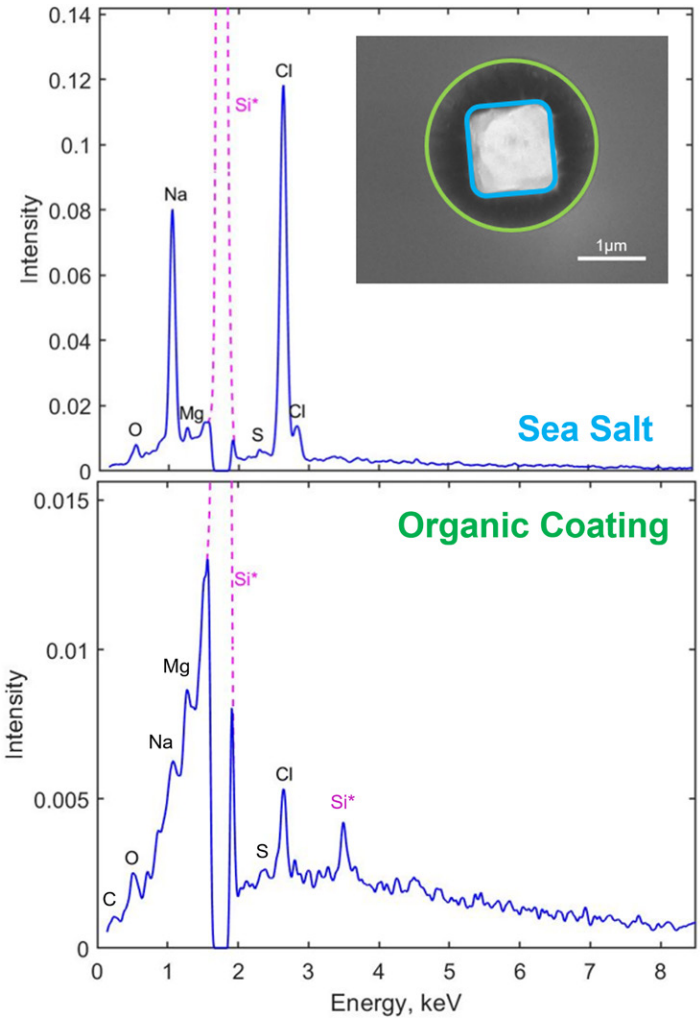

FIG. 9. SEM image (1-μm scale bar) and EDX spectra of the (top) inner sea salt core and (bottom) outer organic coating of a single representative locally produced sea spray aerosol particle, collected at the tundra ground site on 11 Apr 2022 during CHACHA. The dashed silicon (Si*) signal is from the silicon substrate, which was placed on stage 5 (1.0–1.8-μm aerodynamic diameter).

Throughout the CHACHA flight period, dropsondes were released to profile the atmospheric thermal structure, moisture content, and wind speed down to the surface. The air sampling strategy allowed us to study ABL thermodynamics upwind, over, and downwind of leads, with a primary focus on the leads just west of the city of Utqiaġvik (Fig. 11). Dropsondes produced a unique and rare dataset for this environment. Results indicate that statically stable ABLs prevailed over snow-covered and frozen sea ice, with virtual potential temperature gradients reaching 15°C km^{-1} and specific humidity values of approximately 0.1 g (water vapor) per kilogram (air). Air layers close to the sea ice experienced air temperatures as low as −35°C. Over the snow-covered surface and sea ice, thermal inversions persisted throughout the ABL during the CHACHA field campaign. In contrast, over the open water associated with leads,

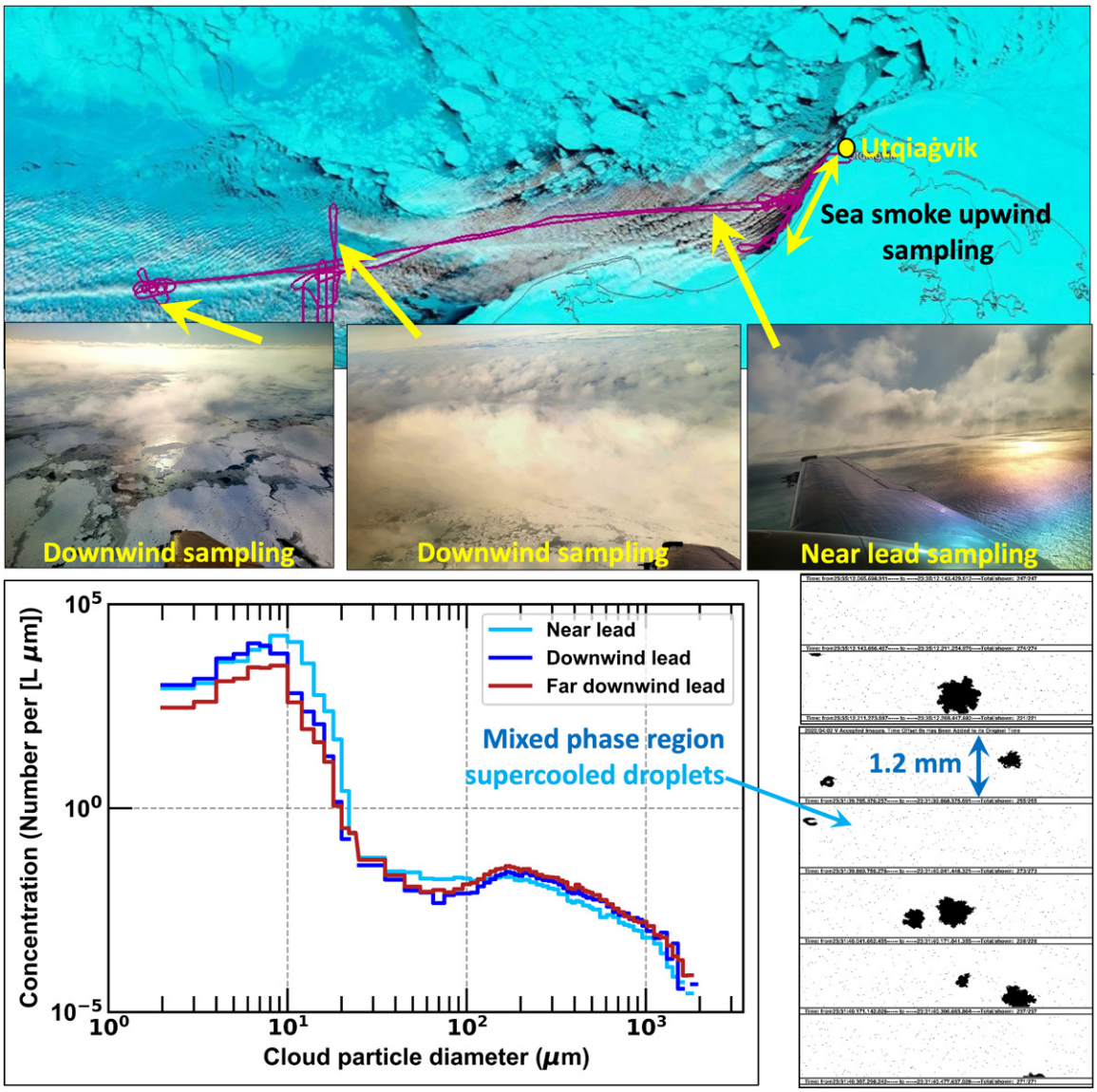

Fig. 10. (top) The satellite image shows the extent of the lead that developed on 2 Apr 2022, west of Utqiaġvik, AK, overlaid with the corresponding flight track flown by the King Air. The images display types of clouds that developed directly overhead and downwind of the leads. Composite in situ cloud PSDs, averaged over the "near-lead," "downwind," and "far downwind" dropsonde locations are shown as colored lines. Nearest the lead, the supercooled droplets were higher in concentration and larger in size, decreasing in both size and concentration as the distance from the lead increases. Conversely, the ice particle mode was lower in concentration and size closest to the lead, but the ice particles grew larger and more numerous with distance downwind, indicative of glaciation as the clouds were advected away from the open lead.

convective and moist layers developed in response to the source of moisture and energy from open water (Fig. 10). The depth of the convective boundary layer reached 250–800 m (Fig. 10), depending on the fetch of leads. Relatively warm and moist plumes emanating from leads warmed overlying air layers by an average of 10°C compared to adjacent air over the sea ice. The convective, moist ABL over leads had specific humidity values that exceeded those of adjacent air layers over the sea ice by 1.0–1.5 g kg^{-1}, while layers above sea ice had less than 0.1 g kg^{-1}. These atmospheric thermodynamic changes in the ABL caused by leads not only impact the transport of energy and moisture but also affect cloud formation and chemical processing both over and downwind of leads. Based on the virtual potential temperature θ_V observed over ice/snow and leads, we estimated the kinematic virtual heat flux ($\overline{w'\theta'_V}$). For convective mixed layers (Z_i) with no heat entrainment, we estimated $\overline{w'\theta'_V}$ above leads.

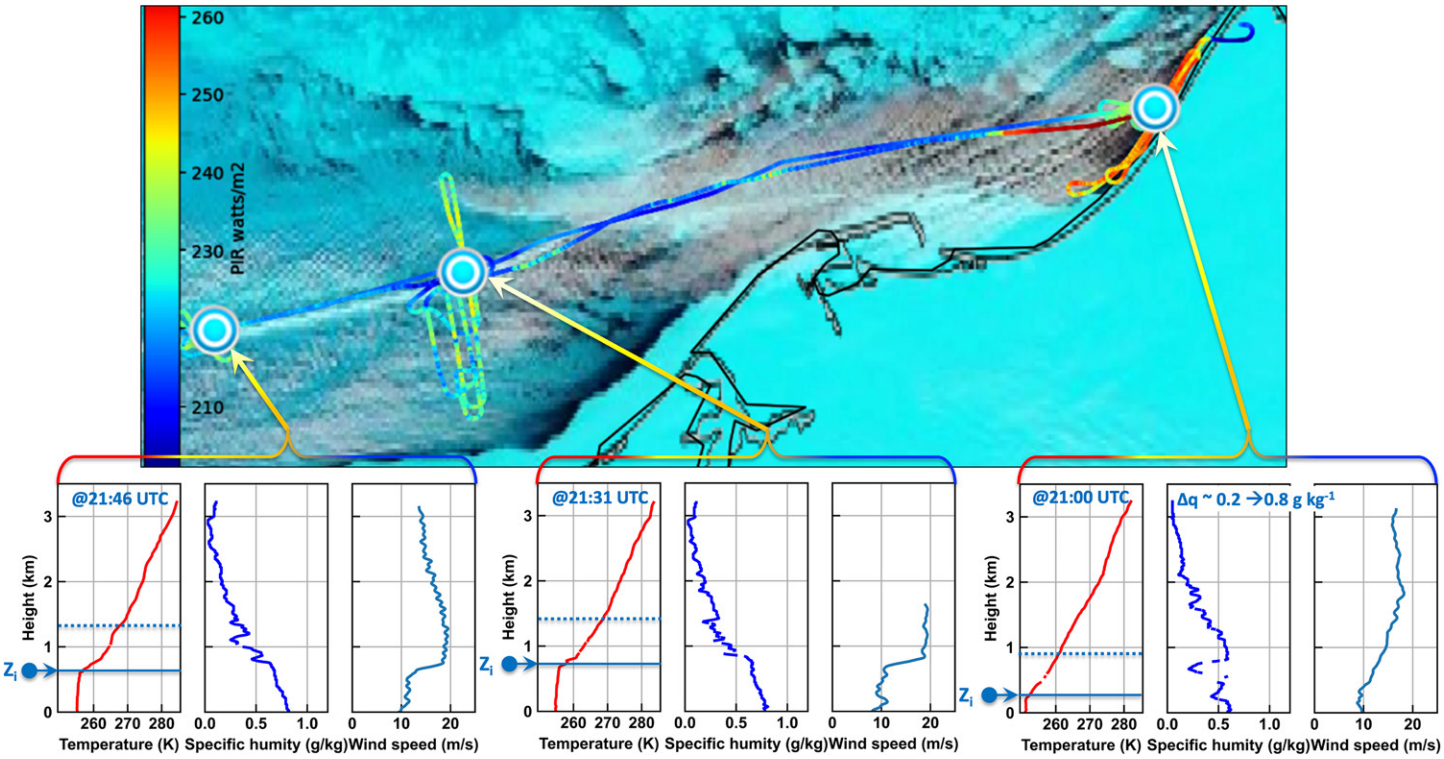

FIG. 11. The map shows characteristics of a lead that formed west of Utqiaġvik, Alaska, on 2 Apr 2022, in the Chukchi Sea. The plots display vertical variations in virtual potential temperature (K), specific humidity (g kg^{-1}), and wind speed (m s^{-1}) over air layers at the start of the lead (upwind), between the start and downwind regions of the lead, and downwind from the lead. The symbol Z_i represents the depth of the atmospheric convective boundary layer, which reached an altitude of 800 m. Dotted lines indicate the likely top of the clouds.

For Z_i ranging from 250 to 850 m in depth and assuming no heat entrainment (Stull 1988), we estimated $\overline{w'\theta'_V}$ values $\left[Zi^2 = \left(2/\gamma_V\right)\int_{t0}^{t}\left(\overline{w'\theta'_V}\right)\partial t\right]$ varying from 0.05 to 0.09 K m s^{-1} (where t_0 and t are the initial and final integration times, respectively). Combining this energy transport with ABL thermodynamics, we computed the convective velocity scale $\left(w_\star = \left\{g/\theta_V\left[\left(\overline{w'\theta'_V}\right)Z_i\right]\right\}^{1/3}\right)$, resulting in values that ranged from 0.8 to 1.2 m s^{-1} above leads. These $w_\star$ results indicated that leads promoted sufficient levels of atmospheric convection, which resulted in cloud formation above and downwind from leads (Fig. 10).

Leads modified the circulation patterns in the air layers immediately above them. One example of this influence relates to the vertical wind speed (w_{ds}). We estimated w_{ds} values as the difference between theoretical and measured fall rates of dropsondes as per previous methodologies (Wang et al. 2009), $w_{ds} = [(2m_{ds}g)/(C_{ds}A_p\rho)]^{0.5}$, where m_{ds} is the dropsonde mass, g is the gravitational acceleration, C_{ds} is the dropsonde drag coefficient, ρ is the air density, and A_p is the cross-sectional area of the parachute (~929 cm^2). As shown in the w_{ds} data (Fig. 12), convection dominated in the first 500 m of the ABL, characterized by upward ($w_{ds} > 0$ m s^{-1}) and downward ($w_{ds} < 0$ m s^{-1}) motions. As dropsondes descended through the air layer extending from the surface to ~1000 m, they encountered alternating updrafts and downdrafts associated with convective cells over leads. Large-eddy simulation (LES) results (e.g., Gryschka et al. 2023) likewise indicate strong updrafts over leads and compensating downdrafts at the cell edges, with inflow from the sides of leads ensuring mass continuity. In addition, dropsondes traversed turbulent layers that frequently exhibited positive ($\partial U/\partial z > 0$ ms^{-1}) and negative ($\partial U/\partial z < 0$ ms^{-1}) wind shear, and U is the horizontal wind speed (Figs. 7 and 11). Such shear displaced the instrument upward or downward, facilitated by the parachute. Together, shear-driven and convective motions produced w_{ds} values ranging from –2 to 2 m s^{-1} (Fig. 12),

consistent with previous studies (Wang et al. 2009; Vömel et al. 2023). These motions facilitated the vertical transport of moist, warm air from leads into the overlying atmosphere, thereby contributing to cloud formation (Fig. 10).

4. Summary

The CHACHA project afforded us the rare opportunity to improve our understanding of how rapid changes associated with climate shifts in the Arctic impact cloud formation, atmospheric gas and aerosol chemical composition, and the thermodynamics of the Arctic ABL during the transition from winter to spring, when sea ice fracturing is common over the Chukchi and Beaufort Seas. During late winter, the ABL above snow/ice-covered regions became dominated by statically stable conditions, with strong thermal inversions that inhibited vertical air parcel mixing. We obtained unique sample and datasets to evaluate the three hypotheses posed regarding aerosols, clouds, and halogens. Arctic leads were not only sources of warm and moist plumes but also of chemically complex, organic-coated sea spray aerosols, as observed previously (Kirpes et al. 2019; Mirrielees et al. 2024). Immediately above and downwind of leads, convective mixing and stratiform and shallow clouds prevailed, with vertical thickness often reaching 300 m. Above leads, clouds took on the appearance of "sea smoke." Within these clouds (starting at ~100 m above the surface), cloud particle concentration spectra exhibited a bimodal distribution, with supercooled droplets (diameter < 30 μm) reaching concentrations of 104 droplets per liter and much smaller concentrations of ice particles (diameter ranging from 100 to 1000 μm). The air within the clouds became turbulent, with updrafts and downdrafts often reaching speeds of up to ±3 m s^{-1}. Measurements of atmospheric particle and cloud chemical composition are ongoing.

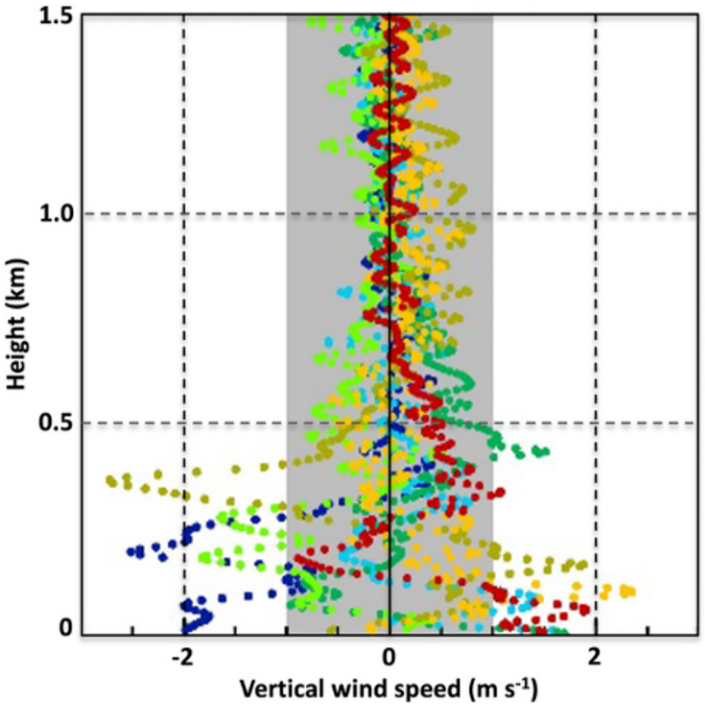

Fig. 12. Vertical wind speed for selected dropsondes over leads. In the air layer extending from the surface to about 500 m, vertical velocity values, ranging from –2 to 2 m s^{-1}, indicate appreciable convective motions associated with updrafts and downdrafts immediately above leads. The gray shaded area indicates the estimated uncertainty in the derived vertical wind speed. Figure adapted from Vömel et al. (2022).

For sunlit conditions above the Arctic tundra snowpack and the snow-covered sea ice, bromine chemistry, as measured from BrO observations, was localized in the near-surface environment, with mixing ratios dropping off rapidly, from as much as 50-ppt BrO near the surface to below 10 ppt at 250-m altitude (Brockway et al. 2024). In the case investigated herein, BrO was elevated and O_3 was depleted, with little apparent distinction between the snow-covered sea ice regions and the snow-covered coastal tundra. However, Brockway et al. (2024) showed that the snow-covered sea ice regions more frequently featured higher surface BrO levels, compared to the snow-covered tundra. Regardless, as in prior studies (Simpson et al. 2005; Pratt et al. 2013; Peterson et al. 2018), reactive bromine chemistry was observed over both snow-covered sea ice and tundra, emphasizing the importance of the propagation of reactive bromine chemistry for hundreds of kilometers inland. The ongoing analysis of

the CHACHA chemical ionization mass spectrometry data is examining the horizontal and vertical extents of active bromine ($HOBr + Br_2$) for further study and comparison to the BrO results.

Emissions of the greenhouse gases methane and carbon dioxide, as well as nitrogen oxides, were quantified from oil and gas extraction within the Prudhoe Bay oil field (Hajny et al. 2025). Notably, we found that the emissions of nitrogen oxides had dramatic impacts on the regional atmospheric chemistry, adding to prior observations of chloride-depleted and nitrate-enriched sea spray aerosols downwind (Kirpes et al. 2018; Gunsch et al. 2017) and within (Gunsch et al. 2020) the oil fields. Observed ambient NO_2 levels ranged from 1 to 10 ppb within the Prudhoe Bay plume, with a maximum NO_2 level of 67 ppb. Locally emitted gases from primary sources remained mostly confined to the air layer extending from the surface to 200 m, reflecting the influence of the shallow, unusually statically stable ABL that suppressed vertical air mixing. Enhanced NO_2 levels in the ABL of the oil fields inhibited bromine radical photochemistry. Horizontal and vertical variations in halogens and oxidants depended on the distribution of point source plumes, as evidenced by suppressed BrO levels in areas dominated by elevated NO_2, as observed during one prior oil field flight transect during the Bromine, Ozone, and Mercury Experiment (BROMEX) campaign in 2012 (Custard et al. 2015). Ongoing investigation of the chemical ionization mass spectrometry measurements of active bromine ($HOBr + Br_2$) and gaseous nitric acid (HNO_3) will yield further insights into this coupled reactive bromine and NO_x chemistry. Because of the reduced atmospheric mixing observed, these NO_x plumes can be transported and detected hundreds of kilometers downwind (Jaffe et al. 1995), resulting in similar suppression of BrO downwind (Peterson et al. 2025). Reaction of BrO with NO_2 forms $BrONO_2$, which reacts on aerosols and the snowpack to form Br_2 and nitrate (NO_3^-). This reaction is generally a NO_x sink, but it can also be a reservoir through snowpack nitrate photolysis and subsequent NO_x emission (France et al. 2012). Snowpack nitrate is also expected from the deposition of nitrate-containing aerosol particles and gaseous HNO_3. Together, these pathways provide an explanation for elevated snowpack nitrate concentrations previously measured between Prudhoe Bay and the Brooks Range (Jaffe and Zukowski 1993). The observed Prudhoe Bay oil field NO_x emissions also result in the formation of peroxynitric acid (HO_2NO_2) and dinitrogen pentoxide (N_2O_5), which has been observed at elevated levels downwind of the oil fields, resulting in enhanced reactive chlorine chemistry (Baker et al. 2016; McNamara et al. 2019, 2021). It is clear that there are a myriad of impacts of the oil field NO_x emissions on multiphase halogen and nitrogen chemistry, and thereby atmospheric oxidation processes, with expected impacts on the oxidation and fate of volatile organic compounds also emitted from the oil fields.

The CHACHA field campaign provided an unprecedented opportunity to determine the extent to which leads modify the thermodynamics of the regional ABL in response to the transport of moist and warm air plumes. For the first time, we investigated the in situ atmospheric thermodynamics of the ABL immediately above leads. Over the snow-covered surface and sea ice, thermal inversions with temperature gradients reaching 15°C km^{-1} persisted throughout the ABL during the field campaign, with specific humidity values of ~0.1 g kg^{-1}. In contrast, over the open water associated with leads, convective and moist air layers developed. The depth of the convective boundary layer ranged from 250 to 850 m, depending on the fetch of the leads. Warm and moist plumes emanating from leads heated the overlying air layers by an average of 10°C compared to the adjacent air layers over the sea ice. The convective, moist boundary layer over leads had specific humidity values ranging from 1.0 to 1.5 g kg^{-1}, compared to less than 0.1 g kg^{-1} in the adjacent air layers over sea ice.

In summary, the CHACHA field campaign generated extensive datasets documenting how changes in the Arctic impact the chemical composition, cloud characteristics, physical structure, and thermodynamics of the Arctic atmospheric boundary layer during spring, following

polar sunrise, and with increasing sea ice fracturing. These datasets are producing an improved understanding of the interactions between sea spray aerosols, surface-coupled clouds, oil field emissions, and multiphase halogen chemistry in the new Arctic. Additionally, they will facilitate the development and testing of numerical models (e.g., Maroneze et al. 2024; Polasky et al. 2024) designed to assess the impacts of anthropogenic changes, such as oil and gas extraction emissions, on the chemical processing of halogens in the Arctic. Relevant data are available through arcticdata.io (https://doi.org/10.18739/A2N58CN8R). Preliminary data are also publicly available on the NCAR field catalog (Costanza 2023).

Acknowledgments. The National Science Foundation supported the CHACHA field campaign (Grants NSF-2001449, NSF-2000493, NSF-2000428, NSF-2000408, NSF-2000403, and NSF-2000404). The CHACHA field campaign was made possible in part due to the support of the University of Wyoming faculty, staff, pilots, and crew of the Wyoming King Air—especially Tom Drew, Ed Sigel, Anna Robertson, Brent Glover, Zane Little, Matt Burkhart, Nick Mahon, Jeff Snider, Larry Oolman, Bart Geerts, Jeff French, and Al Rodi. Raelene Wentz, Cody Johnson, and staff of Ukpeaġvik Iñupiat Corporation (UIC) Science provided support for field operations. We acknowledge additional CHACHA participants that contributed to field preparations and/or support: Andrea Corral, Hannah Kenagy, Kathryn Kulju, Armin Sorooshian, Evelyn Widmaier, and Gracie Wong. We thank Chelsea Thompson from the National Oceanic and Atmospheric Administration (NOAA) Chemical Sciences Laboratory, Boulder, Colorado, for the development of Fig. 1. Jessica Mirrielees is thanked for mentoring Miranda Serratos, who participated in the summer D-RISE program at the University of Michigan; Emily Costa and Vanessa Selimovic are thanked for assistance with Fig. 9. We thank the NOAA, Global Monitoring Laboratory, for the meteorology measurements included in Fig. 4, made at the Utqiaġvik, Alaska, observatory. Authors also thank two anonymous reviewers for their insightful comments, which significantly improved the final version of the manuscript.

Data availability statement. Preliminary datasets are publicly available on the National Science Foundation National Center for Atmospheric Research catalog (Costanza 2023). The resulting datasets will be made available in national and international data banks, such as the Arctic Data Center (https://arcticdata.io/about/).

References

Ahmed, S., and Coauthors, 2022: The role of snow in controlling halogen chemistry and boundary layer oxidation during Arctic spring: A 1D modeling case study. *J. Geophys. Res. Atmos.*, **127**, e2021JD036140, https://doi.org/10.1029/2021JD036140.

Allison, E. H., and H. R. Bassett, 2015: Climate change in the oceans: Human impacts and responses. *Science*, **350**, 778–782, https://doi.org/10.1126/science.aac8721.

Andreas, E. L., C. A. Paulson, R. M. William, R. W. Lindsay, and J. A. Businger, 1979: The turbulent heat flux from Arctic leads. *Bound.-Layer Meteor.*, **17**, 57–91, https://doi.org/10.1007/BF00121937.

Baker, A. K., C. Sauvage, U. R. Thorenz, P. van Velthoven, D. E. Oram, A. Zahn, C. A. Brenninkmeijer, and J. Williams, 2016: Evidence for strong, widespread chlorine radical chemistry associated with pollution outflow from continental Asia. *Sci. Rep.*, **6**, 36821, https://doi.org/10.1038/srep36821.

Barrie, L. A., J. W. Bottenheim, R. C. Schnell, P. J. Crutzen, and R. A. Rasmussen, 1988: Ozone destruction and photochemical reactions at polar sunrise in the lower Arctic atmosphere. *Nature*, **334**, 138–141, https://doi.org/10.1038/334138a0.

Benavent, N., and Coauthors, 2022: Substantial contribution of iodine to Arctic ozone destruction. *Nat. Geosci.*, **15**, 770–773, https://doi.org/10.1038/s41561-022-01018-w.

Bintanja, R., and O. Andry, 2017: Towards a rain-dominated Arctic. *Nat. Climate Change*, **7**, 263–267, https://doi.org/10.1038/nclimate3240.

Bottenheim, J. W., L. A. Barrie, and E. Atlas, 1993: The partitioning of nitrogen oxides in the lower Arctic troposphere during spring 1988. *J. Atmos. Chem.*, **17**, 15–27, https://doi.org/10.1007/BF00699111.

——, J. D. Fuentes, D. W. Tarasick, and K. G. Anlauf, 2002: Ozone in the Arctic lower troposphere during winter and spring 2000 (ALERT2000). *Atmos. Environ.*, **36**, 2535–2544, https://doi.org/10.1016/S1352-2310(02)00121-8.

Brockway, N., and Coauthors, 2024: Tropospheric bromine monoxide vertical profiles retrieved across the Alaskan Arctic in springtime. *Atmos. Chem. Phys.*, **24**, 23–40, https://doi.org/10.5194/acp-24-23-2024.

Cahill, T. A., P. J. Feeney, and R. A. Eldred, 1987: Size-time composition profile of aerosols using the drum sampler. *Nucl. Instrum. Methods Phys. Res., Sect.*, **22B**, 344–348, https://doi.org/10.1016/0168-583X(87)90355-7.

Cavender, A. E., T. A. Biesenthal, J. W. Bottenheim, and P. B. Shepson, 2008: Volatile organic compound ratios as probes of halogen atom chemistry in the Arctic. *Atmos. Chem. Phys.*, **8**, 1737–1750, https://doi.org/10.5194/acp-8-1737-2008.

Chen, Q., J. A. Schmidt, V. Shah, L. Jaeglé, T. Sherwen, and B. Alexander, 2017: Sulfate production by reactive bromine: Implications for the global sulfur and reactive bromine budgets. *Geophys. Res. Lett.*, **44**, 7069–7078, https://doi.org/10.1002/2017GL073812.

——, and Coauthors, 2022: Atmospheric particle abundance and sea salt aerosol observations in the springtime Arctic: A focus on blowing snow and leads. *Atmos. Chem. Phys.*, **22**, 15 263–15 285, https://doi.org/10.5194/acp-22-15263-2022.

Costanza, C., 2023: CHACHA field catalog|NCAR EOL. https://catalog.eol.ucar.edu/chacha.

Crosson, E., 2008: A cavity ring-down analyzer for measuring atmospheric levels of methane, carbon dioxide, and water vapor. *Appl. Phys. B*, **92**, 403–408, https://doi.org/10.1007/s00340-008-3135-y.

Custard, K. D., and Coauthors, 2015: The NO_x dependence of bromine chemistry in the Arctic atmospheric boundary layer. *Atmos. Chem. Phys.*, **15**, 10 799–10 809, https://doi.org/10.5194/acp-15-10799-2015.

——, A. R. W. Raso, P. B. Shepson, R. M. Staebler, and K. A. Pratt, 2017: Production and release of molecular bromine and chlorine from the Arctic coastal snowpack. *ACS Earth Space Chem.*, **1**, 142–151, https://doi.org/10.1021/acsearthspacechem.7b00014.

Faber, S., J. R. French, and R. Jackson, 2018: Laboratory and in-flight evaluation of measurement uncertainties from a commercial Cloud Droplet Probe (CDP). *Atmos. Meas. Tech.*, **11**, 3645–3659, https://doi.org/10.5194/amt-11-3645-2018.

Foster, K., R. Plastridge, J. Bottenheim, P. Shepson, B. Finlayson-Pitts, and C. W. Spicer, 2001: The role of Br_2 and BrCl in surface ozone destruction at polar sunrise. *Science*, **291**, 471–474, https://doi.org/10.1126/science.291.5503.471.

France, J. L., and Coauthors, 2012: Hydroxyl radical and NO_x production rates, black carbon concentrations and light-absorbing impurities in snow from field measurements of light penetration and nadir reflectivity of onshore and offshore coastal Alaskan snow. *J. Geophys. Res.*, **117**, D00R12, https://doi.org/10.1029/2011JD016639.

Frieß, U., H. Sihler, R. Sander, D. Pöhler, S. Yilmaz, and U. Platt, 2011: The vertical distribution of BrO and aerosols in the Arctic: Measurements by active and passive differential optical absorption spectroscopy. *J. Geophys. Res.*, **116**, D00R04, https://doi.org/10.1029/2011JD015938.

Gao, R. S., and Coauthors, 2016: A light-weight, high-sensitivity particle spectrometer for PM2.5 aerosol measurements. *Aerosol Sci. Technol.*, **50**, 88–99, https://doi.org/10.1080/02786826.2015.1131809.

Garman, K. E., and Coauthors, 2006: An airborne and wind tunnel evaluation of a wind turbulence measurement system for aircraft-based flux measurements. *J. Atmos. Oceanic Technol.*, **23**, 1696–1708, https://doi.org/10.1175/JTECH1940.1.

——, P. Wyss, M. Carlsen, J. R. Zimmerman, B. H. Stirm, T. Q. Carney, R. Santini, and P. B. Shepson, 2008: The contribution of variability of lift-induced upwash to the uncertainty in vertical winds determined from an aircraft platform. *Bound.-Layer Meteor.*, **126**, 461–476, https://doi.org/10.1007/s10546-007-9237-y.

General, S., and Coauthors, 2014: The Heidelberg Airborne Imaging DOAS Instrument (HAIDI)—A novel imaging DOAS device for 2-D and 3-D imaging of trace gases and aerosols. *Atmos. Meas. Tech.*, **7**, 3459–3485, https://doi.org/10.5194/amt-7-3459-2014.

Graham, R. M., L. Cohen, A. A. Petty, L. N. Boisvert, A. Rinke, S. R. Hudson, M. Nicolaus, and M. A. Granskog, 2017: Increasing frequency and duration of Arctic winter warming events. *Geophys. Res. Lett.*, **44**, 6974–6983, https://doi.org/10.1002/2017GL073395.

Gryschka, M., V. M. Gryanik, C. Lüpkes, Z. Mostafa, M. Sühring, B. Witha, and S. Raasch, 2023: Turbulent heat exchange over polar leads revisited: A large eddy simulation study. *J. Geophys. Res. Atmos.*, **128**, e2022JD038236, https://doi.org/10.1029/2022JD038236.

Gunsch, M. J., and Coauthors, 2017: Contributions of transported Prudhoe Bay oil field emissions to the aerosol population in Utqiaġvik, Alaska. *Atmos. Chem. Phys.*, **17**, 10 879–10 892, https://doi.org/10.5194/acp-17-10879-2017.

——, J. Liu, C. E. Moffett, R. J. Sheesley, N. Wang, Q. Zhang, T. B. Watson, and K. A. Pratt, 2020: Diesel soot and amine-containing organic sulfate aerosols in an Arctic oil field. *Environ. Sci. Technol.*, **54**, 92–101, https://doi.org/10.1021/acs.est.9b04825.

Hajny, K. D., and Coauthors, 2025: Measurements of the emission rates of nitrogen oxides and greenhouse gases from the Prudhoe Bay oil field. *J. Geophys. Res. Atmos.*, **130**, e2024JD041963, https://doi.org/10.1029/2024JD041963.

Halfacre, J. W., and Coauthors, 2014: Temporal and spatial characteristics of ozone depletion events from measurements in the Arctic. *Atmos. Chem. Phys.*, **14**, 4875–4894, https://doi.org/10.5194/acp-14-4875-2014.

Harsem, Ø., K. Heen, J. M. P. Rodrigues, and T. Vassdal, 2015: Oil exploration and sea ice projections in the Arctic. *Polar Record*, **51**, 91–106, https://doi.org/10.1017/S0032247413000624.

Helmig, D., and Coauthors, 2012: Ozone dynamics and snow-atmosphere exchanges during ozone depletion events at Barrow, Alaska. *J. Geophys. Res.*, **117**, D20303, https://doi.org/10.1029/2012JD017531.

Hornbrook, R. S., and Coauthors, 2016: Arctic springtime observations of volatile organic compounds during the OASIS-2009 campaign. *J. Geophys. Res. Atmos.*, **121**, 9789–9813, https://doi.org/10.1002/2015JD024360.

Jaffe, D. A., and M. D. Zukowski, 1993: Nitrate deposition to the Alaskan snowpack. *Atmos. Environ.*, **27**, 2935–2941, https://doi.org/10.1016/0960-1686(93)90326-T.

——, R. E. Honrath, D. Furness, T. J. Conway, E. Dlugokencky, and L. P. Steele, 1995: A determination of the CH_4, NO_x and CO_2 emissions from the Prudhoe Bay, Alaska oil development. *J. Atmos. Chem.*, **20**, 213–227, https://doi.org/10.1007/BF00694494.

Jeong, D., and Coauthors, 2022: Multiphase reactive bromine chemistry during late spring in the Arctic: Measurements of gases, particles, and snow. *ACS Earth Space Chem.*, **6**, 2877–2887, https://doi.org/10.1021/acsearthspacechem.2c00189.

Jobson, B. T., H. Niki, Y. Yokouchi, J. Bottenheim, F. Hopper, and R. Leaitch, 1994: Measurements of C_2-C_6 hydrocarbons during the Polar Sunrise 1992 experiment: Evidence for Cl atom and Br atom chemistry. *J. Geophys. Res.*, **99**, 25 355–25 368, https://doi.org/10.1029/94JD01243.

Kirpes, R. M., A. L. Bondy, D. Bonanno, R. C. Moffet, B. Wang, A. Laskin, A. P. Ault, and K. A. Pratt, 2018: Secondary sulfate is internally mixed with sea spray aerosol and organic aerosol in the winter Arctic. *Atmos. Chem. Phys.*, **18**, 3937–3949, https://doi.org/10.5194/acp-18-3937-2018.

——, D. Bonanno, N. W. May, M. Fraund, A. J. Barget, R. C. Moffet, A. P. Ault, and K. A. Pratt, 2019: Wintertime Arctic Sea spray aerosol composition controlled by sea ice lead microbiology. *ACS Cent. Sci.*, **5**, 1760–1767, https://doi.org/10.1021/acscentsci.9b00541.

Lance, S., 2012: Coincidence errors in a cloud droplet probe (CDP) and a cloud and aerosol spectrometer (CAS), and the improved performance of a modified CDP. *J. Atmos. Oceanic Technol.*, **29**, 1532–1541, https://doi.org/10.1175/JTECH-D-11-00208.1.

——, C. A. Brock, D. Rogers, and J. A. Gordon, 2010: Water droplet calibration of the Cloud Droplet Probe (CDP) and in-flight performance in liquid, ice and mixed-phase clouds during ARCPAC. *Atmos. Meas. Tech.*, **3**, 1683–1706, https://doi.org/10.5194/amt-3-1683-2010.

——, and Coauthors, 2011: Cloud condensation nuclei as a modulator of ice processes in Arctic mixed-phase clouds. *Atmos. Chem. Phys.*, **11**, 8003–8015, https://doi.org/10.5194/acp-11-8003-2011.

Lata, N. N., Z. Chen, D. Dexheimer, D. Zhang, F. Mei, and S. China, 2023: Vertical gradient of size-resolved aerosol compositions over the Arctic reveals cloud processed aerosol in-cloud and above cloud. *Environ. Sci. Technol.*, **57**, 5821–5830, https://doi.org/10.1021/acs.est.2c09498.

Lawson, R. P., 2011: Effects of ice particles shattering on the 2D-S probe. *Atmos. Meas. Tech.*, **4**, 1361–1381, https://doi.org/10.5194/amt-4-1361-2011.

——, D. O'Connor, P. Zmarzly, K. Weaver, B. Baker, Q. Mo, and H. Jonsson, 2006: The 2D-S (stereo) probe: Design and preliminary tests of a new airborne, high-speed, high-resolution particle imaging probe. *J. Atmos. Oceanic Technol.*, **23**, 1462–1477, https://doi.org/10.1175/JTECH1927.1.

Leck, C., M. Norman, E. K. Bigg, and R. Hillamo, 2002: Chemical composition and sources of the high Arctic aerosol relevant for cloud formation. *J. Geophys. Res.*, **107**, 4135, https://doi.org/10.1029/2001JD001463.

Li, X., S. K. Krueger, C. Strong, G. G. Mace, and S. Benson, 2020: Midwinter Arctic leads form and dissipate low clouds. *Nat. Commun.*, **11**, 206, https://doi.org/10.1038/s41467-019-14074-5.

Liao, J., and Coauthors, 2011: A comparison of Arctic BrO measurements by chemical ionization mass spectrometry and long path-differential optical absorption spectroscopy. *J. Geophys. Res.*, **116**, D00R02, https://doi.org/10.1029/2010JD014788.

——, and Coauthors, 2014: High levels of molecular chlorine in the Arctic atmosphere. *Nat. Geosci.*, **7**, 91–94, https://doi.org/10.1038/ngeo2046.

Lindsay, R. W., and D. A. Rothrock, 1995: Arctic sea ice leads from advanced very high resolution radiometer images. *J. Geophys. Res.*, **100**, 4533–4544, https://doi.org/10.1029/94JC02393.

Liu, J., and Coauthors, 2021: Hydroxymethanesulfonate (HMS) formation during summertime fog in an Arctic oil field. *Environ. Sci. Technol. Lett.*, **8**, 511–518, https://doi.org/10.1021/acs.estlett.1c00357.

Maahn, M., G. de Boer, J. M. Creamean, G. Feingold, G. M. McFarquhar, W. Wu, and F. Mei, 2017: The observed influence of local anthropogenic pollution on northern Alaskan cloud properties. *Atmos. Chem. Phys.*, **17**, 14 709–14 726, https://doi.org/10.5194/acp-17-14709-2017.

——, T. Goren, M. D. Shupe, and G. de Boer, 2021: Liquid containing clouds at the North Slope of Alaska demonstrate sensitivity to local industrial aerosol emissions. *Geophys. Res. Lett.*, **48**, e2021GL094307, https://doi.org/10.1029/2021GL094307.

Marcq, S., and J. Weiss, 2012: Influence of sea ice lead-width distribution on turbulent heat transfer between the ocean and the atmosphere. *Cryosphere*, **6**, 143–156, https://doi.org/10.5194/tc-6-143-2012.

Maroneze, R., F. D. Costa, L. Mortarini, A. D. Polasky, J. D. Fuentes, and O. C. Acevedo, 2024: The role of the turbulent heat flux parameterization on simulating the low level jet intensity using WRF. *15th Conf. Weather, Water, Climate, and the New Energy Economy*, Baltimore, MD, Amer. Meteor. Soc., 16.2, https://ams.confex.com/ams/104ANNUAL/webprogram/Paper439032.html.

May, N. W., P. K. Quinn, S. M. McNamara, and K. A. Pratt, 2016: Multiyear study of the dependence of sea salt aerosol on wind speed and sea ice conditions in the coastal Arctic. *J. Geophys. Res. Atmos.*, **121**, 9208–9219, https://doi.org/10.1002/2016JD025273.

McNamara, S. M., and Coauthors, 2019: Springtime nitrogen oxide-influenced chlorine chemistry in the coastal Arctic. *Environ. Sci. Technol.*, **53**, 8057–8067, https://doi.org/10.1021/acs.est.9b01797.

——, and Coauthors, 2020: Bromine chloride in the coastal Arctic: Diel patterns and production mechanisms. *ACS Earth Space Chem.*, **4**, 620–630, https://doi.org/10.1021/acsearthspacechem.0c00021.

——, Q. Chen, J. Edebeli, K. D. Kulju, J. Mumpfield, J. D. Fuentes, S. B. Bertman, and K. A. Pratt, 2021: Observation of N_2O_5 deposition and $ClNO_2$ production on the saline snowpack. *ACS Earth Space Chem.*, **5**, 1020–1031, https://doi.org/10.1021/acsearthspacechem.0c00317.

Mirrielees, J. A., and Coauthors, 2024: Marine aerosol generation experiments in the high Arctic during summertime. *Elementa*, **12**, 00134, https://doi.org/10.1525/elementa.2023.00134.

Moore, C. W., D. Obrist, A. Steffen, R. M. Staebler, T. A. Douglas, A. Richter, and S. V. Nghiem, 2014: Convective forcing of mercury and ozone in the Arctic boundary layer induced by leads in sea ice. *Nature*, **506**, 81–84, https://doi.org/10.1038/nature12924.

Neuman, J. A., and Coauthors, 2010: Bromine measurements in ozone depleted air over the Arctic Ocean. *Atmos. Chem. Phys.*, **10**, 6503–6514, https://doi.org/10.5194/acp-10-6503-2010.

Nilsson, E. D., Ü. Rannik, E. Swietlicki, C. Leck, P. P. Aalto, J. Zhou, and M. Norman, 2001: Turbulent aerosol fluxes over the Arctic Ocean: 2. Wind-driven sources from the sea. *J. Geophys. Res.*, **106**, 32 139–32 154, https://doi.org/10.1029/2000JD900747.

Olson, N. E., and Coauthors, 2019: Lake spray aerosol incorporated into Great Lakes clouds. *ACS Earth Space Chem.*, **3**, 2765–2774, https://doi.org/10.1021/acsearthspacechem.9b00258.

Oltmans, S. J., and W. D. Komhyr, 1986: Surface ozone distributions and variations from 1973–1984: Measurements at the NOAA geophysical monitoring for climatic change baseline observatories. *J. Geophys. Res.*, **91**, 5229–5236, https://doi.org/10.1029/JD091iD04p05229.

——, B. J. Johnson, and J. M. Harris, 2012: Springtime boundary layer ozone depletion at Barrow, Alaska: Meteorological influence, year-to-year variation, and long-term change. *J. Geophys. Res.*, **117**, D00R18, https://doi.org/10.1029/2011JD016889.

Orellana, M. V., P. A. Matrai, C. Leck, C. D. Rauschenberg, A. M. Lee, and E. Coz, 2011: Marine microgels as a source of cloud condensation nuclei in the high Arctic. *Proc. Natl. Acad. Sci. USA*, **108**, 13 612–13 617, https://doi.org/10.1073/pnas.1102457108.

Orsini, D. A., Y. Ma, A. Sullivan, B. Sierau, K. Baumann, and R. J. Weber, 2003: Refinements to the particle-into-liquid sampler (PILS) for ground and airborne measurements of water soluble aerosol composition. *Atmos. Environ.*, **37**, 1243–1259, https://doi.org/10.1016/S1352-2310(02)01015-4.

Overland, J. E., and M. Wang, 2013: When will the summer Arctic be nearly sea ice free? *Geophys. Res. Lett.*, **40**, 2097–2101, https://doi.org/10.1002/grl.50316.

Peters, G. P., T. B. Nilssen, L. Lindholt, M. S. Eide, S. Glomsrød, L. I. Eide, and J. S. Fuglestvedt, 2011: Future emissions from shipping and petroleum activities in the Arctic. *Atmos. Chem. Phys.*, **11**, 5305–5320, https://doi.org/10.5194/acp-11-5305-2011.

Peterson, P. K., and Coauthors, 2015: Dependence of the vertical distribution of bromine monoxide in the lower troposphere on meteorological factors such as wind speed and stability. *Atmos. Chem. Phys.*, **15**, 2119–2137, https://doi.org/10.5194/acp-15-2119-2015.

——, and Coauthors, 2016: The role of open lead interactions in atmospheric ozone variability between Arctic coastal and inland sites. *Elementa*, **4**, 000109, https://doi.org/10.12952/journal.elementa.000109.

——, and Coauthors, 2017: Observations of bromine monoxide transport in the Arctic sustained on aerosol particles. *Atmos. Chem. Phys.*, **17**, 7567–7579, https://doi.org/10.5194/acp-17-7567-2017.

——, and Coauthors, 2018: Springtime bromine activation over coastal and inland Arctic snowpacks. *ACS Earth Space Chem.*, **2**, 1075–1086, https://doi.org/10.1021/acsearthspacechem.8b00083.

——, K. Pratt, P. Shepson, and W. Simpson, 2025: Impacts of Arctic oil field NO_X emissions on downwind bromine chemistry: Insights from 5 years of MAX-DOAS observations. *Faraday Discuss.*, **258**, 293–306, https://doi.org/10.1039/d4fd00164h.

Platt, U., and T. Wagner, 1998: Satellite mapping of enhanced BrO concentrations in the troposphere. *Nature*, **395**, 486–490, https://doi.org/10.1038/26723.

Polasky, A. D., and Coauthors, 2024: Evaluation of atmospheric boundary layer parameterizations to estimate energy and mass transport in the Arctic using the WRF model. *26th Conf. Atmospheric Chemistry*, Baltimore, MD, Amer. Meteor. Soc., 2C.5, https://ams.confex.com/ams/104ANNUAL/meetingapp.cgi/Paper/436093.

Pratt, K. A., 2019: Tropospheric halogen photochemistry in the rapidly changing Arctic. *Trends Chem.*, **1**, 545–548, https://doi.org/10.1016/j.trechm.2019.06.001.

——, and Coauthors, 2013: Photochemical production of molecular bromine in Arctic surface snowpacks. *Nat. Geosci.*, **6**, 351–356, https://doi.org/10.1038/ngeo1779.

Previdi, M., K. L. Smith, and L. M. Polvani, 2021: Arctic amplification of climate change: A review of underlying mechanisms. *Environ. Res. Lett.*, **16**, 093003, https://doi.org/10.1088/1748-9326/ac1c29.

Radke, L. F., P. V. Hobbs, and J. E. Pinnons, 1976: Observations of cloud condensation nuclei, sodium-containing particles, ice nuclei and the light-scattering coefficient near Barrow, Alaska. *J. Appl. Meteor.*, **15**, 982–995, https://doi.org/10.1175/1520-0450(1976)015<0982:OOCCNS>2.0.CO;2.

Rantanen, M., A. Y. Karpechko, A. Lipponen, K. Nordling, O. Hyvärinen, K. Ruosteenoja, T. Vihma, and A. Laaksonen, 2022: The Arctic has warmed nearly four times faster than the globe since 1979. *Commun. Earth Environ.*, **3**, 168, https://doi.org/10.1038/s43247-022-00498-3.

Raso, A. R., and Coauthors, 2017: Active molecular iodine photochemistry in the Arctic. *Proc. Natl. Acad. Sci. USA*, **114**, 10 053–10 058, https://doi.org/10.1073/pnas.1702803114.

Raynolds, M. K., and Coauthors, 2014: Cumulative geoecological effects of 62 years of infrastructure and climate change in ice-rich permafrost landscapes, Prudhoe Bay Oilfield, Alaska. *Global Change Biol.*, **20**, 1211–1224, https://doi.org/10.1111/gcb.12500.

Rheinlænder, J. W., H. Regan, P. Rampal, G. Boutin, E. Ólason, and R. Davy, 2024: Breaking the ice: Exploring the changing dynamics of winter breakup events in the Beaufort Sea. *J. Geophys. Res. Oceans*, **129**, e2023JC020395, https://doi.org/10.1029/2023JC020395.

Richter, A., F. Wittrock, M. Eisinger, and J. P. Burrows, 1998: GOME observations of tropospheric BrO in northern hemispheric spring and summer 1997. *Geophys. Res. Lett.*, **25**, 2683–2686, https://doi.org/10.1029/98GL52016.

Richter-Menge, J. A., and S. L. Farrell, 2013: Arctic sea ice conditions in spring 2009–2013 prior to melt. *Geophys. Res. Lett.*, **40**, 5888–5893, https://doi.org/10.1002/2013GL058011.

Rodhe, H., 1990: A comparison of the contribution of various gases to the greenhouse effect. *Science*, **248**, 1217–1219, https://doi.org/10.1126/science.248.4960.1217.

Saiz-Lopez, A., and R. von Glasow, 2012: Reactive halogen chemistry in the troposphere. *Chem. Soc. Rev.*, **41**, 6448–6472, https://doi.org/10.1039/c2cs35208g.

Saunders, P. M., 1964: Sea smoke and steam fog. *Quart. J. Roy. Meteor. Soc.*, **90**, 156–165, https://doi.org/10.1002/qj.49709038405.

Schmale, J., S. R. Arnold, K. S. Law, T. Thorp, S. Anenberg, W. R. Simpson, J. Mao, and K. A. Pratt, 2018: Local Arctic air pollution: A neglected but serious problem. *Earth's Future*, **6**, 1385–1412, https://doi.org/10.1029/2018EF000952.

Schroeder, W. H., K. G. Anlauf, L. A. Barrie, J. Y. Lu, A. Steffen, D. R. Schneeberger, and T. Berg, 1998: Arctic springtime depletion of mercury. *Nature*, **394**, 331–332, https://doi.org/10.1038/28530.

Scott, W. D., and Z. E. V. Levin, 1972: Open channels in sea ice (leads) as ion sources. *Science*, **177**, 425–426, https://doi.org/10.1126/science.177.4047.425.

Seo, S., A. Richter, A. M. Blechschmidt, I. Bougoudis, and J. P. Burrows, 2019: First high-resolution BrO column retrievals from TROPOMI. *Atmos. Meas. Tech.*, **12**, 2913–2932, https://doi.org/10.5194/amt-12-2913-2019.

Serreze, M. C., and R. G. Barry, 2011: Processes and impacts of Arctic amplification: A research synthesis. *Global Planet. Change*, **77**, 85–96, https://doi.org/10.1016/j.gloplacha.2011.03.004.

Shepson, P., and F. Domine, Eds., 2022: *Chemistry in the Cryosphere (in 2 Parts).* Vol. 3, World Scientific, 924 pp.

Shingler, T., and Coauthors, 2012: Characterisation and airborne deployment of a new counterflow virtual impactor inlet. *Atmos. Meas. Tech.*, **5**, 1259–1269, https://doi.org/10.5194/amt-5-1259-2012.

Simpson, W. R., L. Alvarez-Aviles, T. A. Douglas, M. Sturm, and F. Domine, 2005: Halogens in the coastal snow pack near Barrow, Alaska: Evidence for active bromine air-snow chemistry during springtime. *Geophys. Res. Lett.*, **32**, L04811, https://doi.org/10.1029/2004GL021748.

——, D. Carlson, G. Hönninger, T. A. Douglas, M. Sturm, D. Perovich, and U. Platt, 2007a: First-year sea-ice contact predicts bromine monoxide (BrO) levels at Barrow, Alaska better than potential frost flower contact. *Atmos. Chem. Phys.*, **7**, 621–627, https://doi.org/10.5194/acp-7-621-2007.

——, and Coauthors, 2007b: Halogens and their role in polar boundary-layer ozone depletion. *Atmos. Chem. Phys.*, **7**, 4375–4418, https://doi.org/10.5194/acp-7-4375-2007.

——, and Coauthors, 2017: Horizontal and vertical structure of reactive bromine events probed by bromine monoxide MAX-DOAS. *Atmos. Chem. Phys.*, **17**, 9291–9309, https://doi.org/10.5194/acp-17-9291-2017.

Smith, S. D., R. D. Muench, and C. H. Pease, 1990: Polynyas and leads: An overview of physical processes and environment. *J. Geophys. Res.*, **95**, 9461–9479, https://doi.org/10.1029/JC095iC06p09461.

Steffen, A., and Coauthors, 2008: A synthesis of atmospheric mercury depletion event chemistry in the atmosphere and snow. *Atmos. Chem. Phys.*, **8**, 1445–1482, https://doi.org/10.5194/acp-8-1445-2008.

Stroeve, J., and D. Notz, 2018: Changing state of Arctic sea ice across all seasons. *Environ. Res. Lett.*, **13**, 103001, https://doi.org/10.1088/1748-9326/aade56.

Strong, C., J. D. Fuentes, R. E. Davis, and J. W. Bottenheim, 2002: Thermodynamic attributes of Arctic boundary layer ozone depletion. *Atmos. Environ.*, **36**, 2641–2652, https://doi.org/10.1016/S1352-2310(02)00114-0.

Stuecker, M. F., and Coauthors, 2018: Polar amplification dominated by local forcing and feedbacks. *Nat. Climate Change*, **8**, 1076–1081, https://doi.org/10.1038/s41558-018-0339-y.

Stull, R. B., 1988: *An Introduction to Boundary Layer Meteorology.* Kluwer Academic Publishers Group, 670 pp.

Tetzlaff, A., C. Lüpkes, and J. Hartmann, 2015: Aircraft-based observations of atmospheric boundary-layer modification over Arctic leads. *Quart. J. Roy. Meteor. Soc.*, **141**, 2839–2856, https://doi.org/10.1002/qj.2568.

Vömel, H., M. Goodstein, C. Arendt, and J. Witte, 2022: Dropsonde Data Report, Chemistry in the Arctic: Clouds, Halogens, and Aerosols CHACHA (2022). National Center for Atmospheric Research, 22 pp.

——, A. Sorooshian, C. Robinson, T. J. Shingler, K. L. Thornhill, and L. D. Ziemba, 2023: Dropsonde observations during the aerosol cloud meteorology interactions over the western Atlantic experiment. *Sci. Data*, **10**, 753, https://doi.org/10.1038/s41597-023-02647-5.

Wales, P. A., and Coauthors, 2023: Application of satellite-based detections of Arctic bromine explosion events within GEOS-chem. *J. Adv. Model. Earth Syst.*, **15**, e2002MS003465, https://doi.org/10.1029/2022MS003465.

Walker, D. A., and Coauthors, 2022: Cumulative impacts of a gravel road and climate change in an ice-wedge-polygon landscape, Prudhoe Bay, Alaska. *Arct. Sci.*, **8**, 1040–1066, https://doi.org/10.1139/as-2021-0014.

Wang, J., J. Bian, W. O. Brown, H. Cole, V. Grubišić, and K. Young, 2009: Vertical air motion from T-REX radiosonde and dropsonde data. *J. Atmos. Oceanic Technol.*, **26**, 928–942, https://doi.org/10.1175/2008JTECHA1240.1.

Wang, S., and K. A. Pratt, 2017: Molecular halogens above the Arctic snowpack: Emissions, diurnal variations, and recycling mechanisms. *J. Geophys. Res. Atmos.*, **122**, 11 991–12 007, https://doi.org/10.1002/2017JD027175.

——, and Coauthors, 2019: Direct detection of atmospheric atomic bromine leading to mercury and ozone depletion. *Proc. Natl. Acad. Sci. USA*, **116**, 14 479–14 484, https://doi.org/10.1073/pnas.1900613116.

Widmaier, E. M., A. R. Jensen, and K. A. Pratt, 2024: Arctic tropospheric ozone seasonality, depletion, and oil field influence. *Faraday Discuss.*, **258**, 265–292, https://doi.org/10.1039/D4FD00166D.